Monthly Notices of the ROYAL ASTRONOMICAL SOCIETY

MNRAS **521,** 5508–5535 (2023) https://doi.org/10.1093/mnras/stad784
Advance Access publication 2023 March 17

Bright extragalactic ALMA redshift survey (BEARS) III: detailed study of emission lines from 71 *Herschel* targets

M. Hagimoto[1★] T. J. L. C. Bakx[1,2] S. Serjeant[3] G. J. Bendo[4] S. A. Urquhart,[3] S. Eales,[5] K. C. Harrington[6] Y. Tamura[1] H. Umehata,[1,7] S. Berta,[8] A. R. Cooray,[9] P. Cox,[10] G. De Zotti[11] M. D. Lehnert,[12] D. A. Riechers,[13] D. Scott,[14] P. Temi,[15] P. P. van der Werf,[16] C. Yang,[17] A. Amvrosiadis,[18] P. M. Andreani[19] A. J. Baker,[20,21] A. Beelen[23] E. Borsato,[22] V. Buat[23] K. M. Butler,[16] H. Dannerbauer,[24,25] L. Dunne,[5] S. Dye[26] A. F. M. Enia[27,28] L. Fan,[29,30,31] R. Gavazzi,[10,32] J. González-Nuevo,[33,34] A. I. Harris,[35] C. N. Herrera,[8] D. H. Hughes,[36] D. Ismail,[23] R. J. Ivison[19] B. Jones[13] K. Kohno[37,38] M. Krips,[8] G. Lagache,[23] L. Marchetti[39,40] M. Massardi,[40,41] H. Messias[6,42] M. Negrello,[5] R. Neri,[8] A. Omont,[10] I. Perez-Fournon,[24,25] C. Sedgwick,[3] M. W. L. Smith[5] F. Stanley,[10] A. Verma,[43] C. Vlahakis,[44] B. Ward,[5] C. Weiner,[3] A. Weiß[45] and A. J. Young[20]

Affiliations are listed at the end of the paper

Accepted 2023 March 4. Received 2023 January 26; in original form 2022 December 7

ABSTRACT

We analyse the molecular and atomic emission lines of 71 bright *Herschel*-selected galaxies between redshifts 1.4 and 4.6 detected by the Atacama Large Millimeter/submillimeter Array. These lines include a total of 156 CO, [C I], and H_2O emission lines. For 46 galaxies, we detect two transitions of CO lines, and for these galaxies we find gas properties similar to those of other dusty star-forming galaxy (DSFG) samples. A comparison to photodissociation models suggests that most of *Herschel*-selected galaxies have similar interstellar medium conditions as local infrared-luminous galaxies and high-redshift DSFGs, although with denser gas and more intense far-ultraviolet radiation fields than normal star-forming galaxies. The line luminosities agree with the luminosity scaling relations across five orders of magnitude, although the star formation and gas surface density distributions (i.e. Schmidt–Kennicutt relation) suggest a different star formation phase in our galaxies (and other DSFGs) compared to local and low-redshift gas-rich, normal star-forming systems. The gas-to-dust ratios of these galaxies are similar to Milky Way values, with no apparent redshift evolution. Four of 46 sources appear to have CO line ratios in excess of the expected maximum (thermalized) profile, suggesting a rare phase in the evolution of DSFGs. Finally, we create a deep stacked spectrum over a wide rest-frame frequency (220–890 GHz) that reveals faint transitions from HCN and CH, in line with previous stacking experiments.

Key words: galaxies: high-redshift – galaxies: ISM – infrared: galaxies – submillimetre: galaxies.

1 INTRODUCTION

Since the advent of wide-field submillimetre instrumentation, we have been aware of a population of high-redshift dusty star-forming galaxies (DSFGs), which are subdominant at rest-frame optical wavelengths but contribute to the comoving volume-averaged star formation density (e.g. Smail, Ivison & Blain 1997; Hughes et al. 1998; Blain et al. 2002; Casey, Narayanan & Cooray 2014) of 20–80 per cent over most of the history of the Universe (e.g. Zavala et al. 2021), particularly at the *peak* in star formation density at $z \sim 2.5$ (Madau & Dickinson 2014). The *Herschel Space Observatory*, the *Planck* satellite, the South-Pole Telescope (SPT), and the Atacama Cosmology Telescope (ACT) each mapped one to several thousands of square degrees and discovered many high-redshift galaxies apparently forming stars at rates beyond $1000\,M_\odot\ yr^{-1}$ (Rowan-Robinson et al. 2016). However, hydrodynamical models of galaxies initially failed to reproduce these extreme star-forming events (e.g. Narayanan et al. 2015). A further complication is that high-resolution follow-up observations of individual sources reveal a heterogeneous population, from smooth discs to clumpy merger-like systems (e.g. Bussmann et al. 2013, 2015; Dye et al. 2015, 2018; Hodge et al. 2016; Gullberg et al. 2018; Lelli et al. 2021; Chen et al. 2022). Accurate characterization of these diverse sources across larger samples is thus needed, although so far such detailed studies of this population have been limited by the lack of angular resolving power of single-dish telescopes and the intrinsic uncertainty in the photometric redshifts estimated from the far-infrared regime($\Delta z/(1+z) \simeq 0.13$ (Lapi et al. 2011; González-Nuevo et al. 2012; Pearson et al. 2013; Ivison et al. 2016; Bakx et al. 2018).

The large areas of the DSFG surveys allowed the selection of rare types of galaxies. In fact, simply selecting galaxies with 500-μm

★ E-mail: hagimoto@a.phys.nagoya-u.ac.jp

flux densities $S_{500} > 100$ mJy has proven to be a reliable selector of strongly gravitationally lensed systems (Negrello et al. 2007, 2010; Wardlow et al. 2013; Negrello et al. 2014, 2017; Nayyeri et al. 2016). In an effort to better understand bright, distant *Herschel* galaxies, Bakx et al. (2018) selected sources with $S_{500} \geq 80$ mJy, as well as a photometric redshift $z_{\rm phot} \geq 2$, based on the *Herschel*-Spectral and Photometric Imaging Receiver (SPIRE) fluxes, in order to decrease the contamination rate (see also Bakx et al. 2020b). They constructed a sample of 209 sources, known collectively as the *Herschel* Bright Sources (HerBS) sample. A cross-correlation analysis in Bakx, Eales & Amvrosiadis (2020a) has shown it is likely that lower flux criterion (100 mJy $> S_{500} >$ 80 mJy) selects towards more intrinsically bright sources with lower magnification factors. Thus, this sample likely not only includes rare strongly lensed sources, but also intrinsically very bright sources, such as hyperluminous infrared galaxies (HyLIRGS; $L_{\rm IR} > 10^{13}$ L$_\odot$, Fu et al. 2013; Ivison et al. 2013; Riechers et al. 2013, 2017; Oteo et al. 2016).

The angular magnification in the strongly gravitationally lensed sources enables resolved observations of the gas down to 100-pc scales (e.g. Dye et al. 2015; Tamura et al. 2015; Egami et al. 2018) with follow-up imaging. Such observations are well suited to illuminate the physical processes driving the star formation activity within the galaxies, particularly through resolved kinematics of spectral lines. Similarly, resolved gas morphologies and kinematics will hold the key to understanding the physical origin of HyLIRGs. However, determining the spectroscopic redshift of individual sources is an essential first step, and therefore several redshift campaigns have targeted submm- and mm-wave-selected galaxies. In the Northern hemisphere, the Institut de Radio Astronomie Millimetrique (IRAM) 30-m telescope and NOrthern Extended Millimeter Array (NOEMA) have been used to search for CO emission lines for determining spectroscopic redshifts (Bakx et al. 2020c; Neri et al. 2020). In particular, the NOEMA project *z*-GAL (P.I.s: P. Cox, H. Dannerbauer, and T. Bakx) aims to obtain the spectroscopic redshifts of 137 sources in northern and equatorial fields (Cox et al., in preparation). However, a large fraction of the *Herschel* sources in the Southern hemisphere had not yet been done.

Therefore, Urquhart et al. (2022) and Bendo et al. (2023) presented the result of the Bright Extragalactic Atacama Large Millimeter/submillimeter Array (ALMA) Redshift Survey (BEARS). They selected the 85 sources from HerBS that are located in the South Galactic Pole field and previously lacked spectroscopic redshifts. Using a series of meticulously chosen spectral windows, they reported 71 spectroscopic redshifts by targeting the brightest mm-wavelength lines, i.e. the rotational transitions of CO (J, $J-1$) (see Bakx & Dannerbauer 2022). These observations have angular resolutions of ∼2–3 arcsec for the 2 and 3 mm spectral windows, respectively. Since higher-J transitions are sensitive to denser and warmer gas, the line luminosity ratios between different transitions can provide insight into the gas conditions within the galaxies such as gas densities and kinetic temperatures (e.g. Weiß et al. 2007; Bothwell et al. 2013; Yang et al. 2017; Cañameras et al. 2018; Dannerbauer et al. 2019; Harrington et al. 2021). Furthermore, lines with a high critical density and temperature are excited for the strongly lensed, high-redshift *Planck* selected sources, indicating molecular gas is typically warmer for these dusty star-forming systems with high intrinsic infrared luminosities (∼$\log_{10}L_{\rm IR} = 12.5$–$13.7$ L$_\odot$; Harrington et al. 2021). Similar findings have been reported for the SPT-selected sources (Reuter et al. 2020) and studies of bright *Herschel* galaxies (Yang et al. 2017; Bakx et al. 2020c; Neri et al. 2020).

The CO lines from this redshift search provide us with a sensitive probe of the interstellar medium (ISM) conditions of a large sample of *Herschel* galaxies. Specifically, the Schmidt–Kennicutt (SK) relation between the star formation surface density and molecular gas mass ($\Sigma_{\rm SFR}$–$\Sigma_{\rm H_2}$; Schmidt 1959; Kennicutt 1998) is diagnostic of the star formation mode, i.e. 'main sequence' as opposed to 'starburst'. High-redshift dusty starbursts typically have higher star formation rates (SFRs) relative to their molecular gas compared to normal star-forming galaxies (e.g. Casey et al. 2014), which results in a shorter depletion time-scale (∼100 Myr). The reasons for this boost in star formation are often hypothesized to be connected with recent merger events (Sanders et al. 1988; Barnes & Hernquist 1991; Hopkins et al. 2008), although several other theories have been posited (Cai et al. 2013; Gullberg et al. 2019; Hodge et al. 2019; Rizzo et al. 2020; Fraternali et al. 2021). CO is the second-most abundant molecule in the ISM, and the $J = 1$–0 transition to the ground state has traditionally been considered as the best tracer of the molecular gas mass. However, it is difficult to observe in high-redshift galaxies due to its relative faintness. Alternatively, other low-J CO lines, such as CO (2–1) or (3–2), can be used as molecular gas tracers, although to use these we have to assume a gas excitation. In addition, we could miss the molecular gas mass behind the 'photosphere' due to the optically thick nature of ^{12}CO, particularly for low-J CO lines. In this situation, the [C I] ($^3P_1$–$^3P_0$) line is a useful alternative tracer, which has been discussed from both theoretical and observational perspectives (e.g. Papadopoulos & Greve 2004; Papadopoulos, Thi & Viti 2004). [C I] ($^3P_1$–$^3P_0$) is typically optically thin and therefore probes the full molecular gas mass, although in the local Universe there exists not much difference between molecular gas estimates from CO lines and [C I] ($^3P_1$–$^3P_0$) (Israel 2020). In addition, it is a useful probe of the physical conditions of the photodissociation regions (PDRs) inside these dusty starbursts (e.g. Alaghband-Zadeh et al. 2013; Bothwell et al. 2017; Jiao et al. 2017; Valentino et al. 2020b).

In this paper, we exploit the 156 detections and upper limits of CO rotational transitions, as well as [C I] atomic carbon and the H_2O (2_{11}–2_{02}) water transition within the BEARS project to estimate the ISM conditions of 71 bright *Herschel*-selected galaxies. We briefly describe the sample and observations in Section 2, and show the initial sample results in Section 3. We discuss these results in Section 4, Section 5 discusses four sources with strange spectral features, and Section 6 discusses the composite spectrum. We provide our main conclusions in Section 7. Throughout this paper, we adopted a spatially flat ΛCDM cosmology with the best-fitting parameters derived from the *Planck* results (Planck Collaboration XIII 2016), which are $\Omega_{\rm m} = 0.307$, $\Omega_\Lambda = 0.693$, and $h = 0.693$.

2 SAMPLE AND OBSERVATIONS

Our sources are selected from the *Herschel* Bright Sources sample (HerBS; Bakx et al. 2018, 2020b), which contains the 209 brightest, high-redshift sources in the 616.4 deg^2, H-ATLAS survey (Eales et al. 2010). The H-ATLAS survey used the PACS (Poglitsch et al. 2010) and SPIRE (Griffin et al. 2010) instruments on *Herschel* to observe the North and South Galactic Pole Fields, as well as three equatorial fields, to a 1σ sensitivity of 5.2 mJy at 250 μm to 6.8 mJy at 500 μm. [1] (Eales et al. 2010; Valiante et al. 2016). The sources are selected with a photometric redshift, $z_{\rm phot}$, greater than 2 and a 500-μm flux density, S_{500}, greater than 80 mJy. Blazar contaminants were removed with radio catalogues and verified with 850- μm SCUBA-2

[1]These sensitivities are derived from the background-subtracted, matched-filtered maps without accounting for confusion noise.

observations (Bakx et al. 2018). The infrared photometric redshift of each source was initially calculated through the fitting of a two-temperature modified blackbody (MBB) spectral energy distribution template from Pearson et al. (2013) to the 250-, 350-, and 500- μm flux densities (Bakx et al. 2018). This MBB was derived from the *Herschel*-SPIRE photometry of 40 lensed H-ATLAS sources with spectroscopic redshifts from the H-ATLAS survey, and assumed both a cold (23.9 K) and warm (46.9 K) component of the dust. These sources are similar to the ones in this sample, and would thus provide a good initial photometric redshift estimate, with an estimated error of $\Delta z/(1+z) \approx 0.12$. Improved photometric fits of the data, including the recent ALMA data, are reported in Bendo et al. (2023).

Concerted efforts have been made to measure the redshifts of these sources using both single-dish telescopes (e.g. IRAM; Bakx et al. 2020c) and interferometers (e.g. NOEMA; Neri et al. 2020). However, most of the sources in the Southern hemisphere have been out of reach for earlier redshift search attempts with CARMA, NOEMA, and IRAM 30-m. As described by Urquhart et al. (2022), our targeted sources are all located in the South Galactic Pole field (Eales et al. 2010). The initial line searches were conducted by the Atacama Compact Array (ACA; also called the Morita Array) for 11 sources in the 3-mm band (Band 3). This has been complemented by a larger scale search using the 12-m Array that observed another 74 sources at 3 mm, and all 85 targets at 2 mm, in an effort to measure robust redshifts. In total, the redshifts of 71 galaxies in 62 out of 85 *Herschel* fields were identified. The redshift identification is described in more detail in Urquhart et al. (2022), with the continuum and source-multiplicity analysis presented in Bendo et al. (2023).

3 LINE FLUXES

We use the line fluxes reported in Urquhart et al. (2022) for all detected lines, which we complement with upper-limit extractions using the following method. Briefly, for the detected lines, circular apertures were centred on the peaks of the corresponding continuum emission, and the radii of the apertures were manually adjusted for each source in each image to include as much line emission as possible while still measuring that emission at higher than the 5σ level. These apertures were several times larger than the beam size, removing potential bias when comparing lines with different signal-to-noise ratios or with different beam sizes. Similarly, the frequency channels were manually selected such that as much of the line flux as possible was included while still yielding measurements above the 5σ level. For non-detected lines, the same aperture and line velocity width as the detected lines were used. We then fit a Gaussian profile to the frequency of the undetected spectral lines with a fixed velocity width. The resulting uncertainty on this fit then provided us with the 1σ error.

Fig. 1 shows an overview of all the detected spectral lines and the 3σ upper limits of undetected lines of all sources. Most of the detected spectral lines are from CO ranging from $J = 2$–1 to 7–6, and in addition, we detect the [C I] ($^3P_1$–$^3P_0$) line for 23 sources, a water line (H_2O (2_{11}–2_{02})) for two sources, and the [C I] ($^3P_2$–$^3P_1$) line for four sources. We also include the upper limits of a single CO, six [C I] ($^3P_1$–$^3P_0$), and three H_2O (2_{11}–2_{02}) lines. Most of these lines had already been reported in Urquhart et al. (2022), however, we extracted three extra [C I] ($^3P_1$–$^3P_0$), three extra [C I] ($^3P_2$–$^3P_1$), and one extra H_2O (2_{11}–2_{02}) lines. These additional velocity-integrated line fluxes and upper limits are listed in Table A1. We find velocity-integrated fluxes, I_{CO}, ranging from 0.6 to 21.1 Jy km s^{-1}. We do not correct for cosmic microwave background (CMB) effects (i.e. the observational contrast against the CMB and the enhanced excitation of the CO or other line transitions), since this requires extensive modelling of the ISM conditions and exceeds the scope of this paper, particularly since it is not a large correction at these redshifts (da Cunha et al. 2013; Zhang et al. 2016; Tunnard & Greve 2017). The velocity-width full width at half-maximum (FWHM) of our sources ranges between 110 and 1290 km s^{-1}. This observed diversity in line profiles is also seen in the Fig. G1, where the velocity distribution of the BEARS systems is compared against one another.

4 DISCUSSION

4.1 CO spectral line energy distributions

Fig. 2 compares the normalized integrated line intensities for each of the sources. In this figure, the sources are normalized to the expected CO (1–0) line velocity-integrated flux, derived from the mean spectral line energy distribution (SLED) of the turbulent model in Harrington et al. (2021), using the lowest J_{up} CO line with $\pm 1\sigma$ standard deviation (shown as the grey shaded region). The colour of the lines indicates the lowest J_{up} transition, starting from $J_{up} = 2$ to 5 shown in *red, blue, green*, and *orange*. The *dashed lines* show the associated thermalized profiles for each normalized transition ($I_{CO} \propto J_{up}^2$, with the instant of proportionality determined by the SLED from Harrington et al. 2021). The *connected red plus points* indicate the SLED from the stacked spectrum (see Section 6 for details).

The CO SLEDs reflect a diverse population that broadly follows the mean ratios reported by Harrington et al. (2021), which has a slightly smaller median redshift ($z_{med} = 2.4$) relative to our median redshift ($z_{med} = 2.7$). Several sources already show a downward trend in velocity-integrated intensity at $J_{up} < 4$, which is more in line with non-starburst galaxies (Dannerbauer et al. 2009; Boogaard et al. 2020) such as the Milky Way (Fixsen, Bennett & Mather 1999). It is important to note that the general shape of CO SLEDs consists of multiple components (e.g. Daddi et al. 2015; Yang et al. 2017; Cañameras et al. 2018). The stacked SLED straddles the top of the expected ratios from Harrington et al. (2021), but it is normalized only to two CO (2–1) detections and reflects the average line ratios across a wide range in redshifts. The stacked SLED agrees within the 1σ error with the model from Harrington et al. (2021), although it appears higher for $J_{up} > 4$. While the majority of sources show sub-thermalized profiles (i.e. below their respective *dashed lines*), several sources (HerBS-69B, -120A, -120B, -159B) have SLEDs above the typically assumed theoretical maximum excitation, based on the equipartition distribution of the CO excitation states; this will be discussed separately in Section 5.

We provide an alternative perspective on the CO SLEDs of our sources in Fig. 3, where we compare the luminosity ratios of all detected lines. We calculate the line luminosity for the spectral lines using the equation from Solomon et al. (1997):

$$L' = 3.25 \times 10^7 S_{CO}\Delta v f_{obs}^{-2} D_L^2 (1+z)^{-3} \text{ [K km s}^{-1}\text{ pc}^2\text{]}, \quad (1)$$

with the integrated flux, $S_{CO}\Delta v$, in Jy km s^{-1}, the observed frequency, f_{obs}, in GHz, and the luminosity distance, D_L, in Mpc. We derive the line luminosity ratios, r_{J_a,J_b}, for each of our sources, using

$$r_{J_a,J_b} = \frac{L'_a}{L'_b} = \frac{I_a}{I_b}\frac{J_b^2}{J_a^2}. \quad (2)$$

Here, L'_a and L'_b refer to the luminosity of lines a and b, I_a and I_b refer to the integrated line flux, and J_a and J_b refer to the upper rotational quantum level, commonly referred to as J_{up}. We

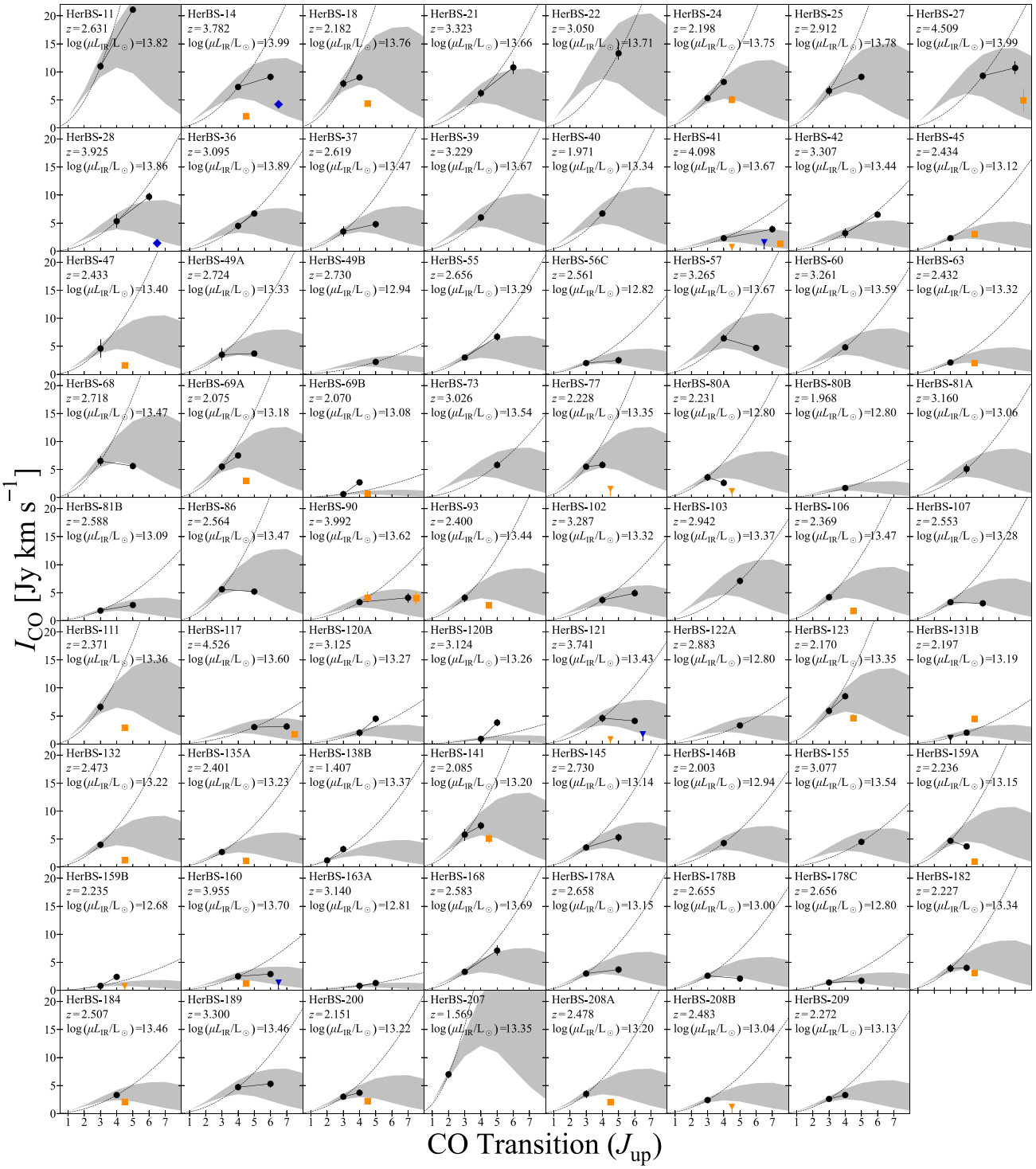

Figure 1. Integrated line intensities of the spectral lines for each of the galaxies with robust spectroscopic redshifts (see Urquhart et al. 2022). We show the CO-line transitions as *connected black points*, and include [C I] ($^3P_1$–$^3P_0$) and [C I] ($^3P_2$–$^3P_1$) as *unconnected orange squares* at $J_{up} = 4.5$ and 7.5, respectively. The *unconnected blue diamond* at $J_{up} = 6.5$ refers to the H_2O (2_{11}–2_{02}) line. The positions of the [C I] and H_2O lines are chosen based on their frequency relative to the CO lines. We show 3σ upper limits as *downward triangles*. The *dashed black line* shows the thermalized SLED profile fitted to the lowest-J_{up} CO transition, and the *filled grey region* shows the mean SLED obtained from the turbulent model for *Planck*-selected galaxies by Harrington et al. (2021) with associated 1σ spread propagated in quadrature, also fitted to the lowest J_{up} CO transition for each galaxy. We also include the source ID, spectroscopic redshift, and apparent infrared luminosity for each panel.

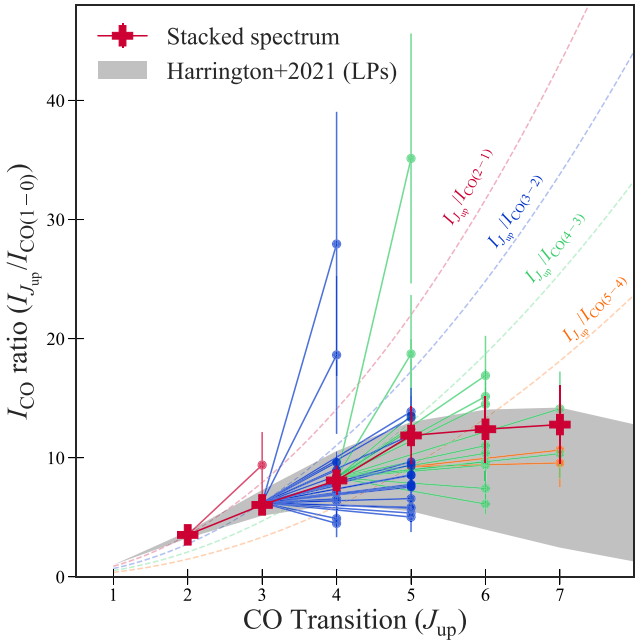

Figure 2. Normalized line intensities of BEARS galaxies against the observed CO line transition. The lines are normalized to the CO (1–0) emission calculated using the mean SLED obtained from the turbulent model for strongly lensed galaxies identified by the *Planck* satelite (LPs) in Harrington et al. (2021). The colour of the marker reflects the lowest J_{up} transition observed to the galaxy. Similarly, the *coloured dashed lines* indicate the thermalized profiles for the lowest transitions ($\propto J_{up}^2$). The *grey filled region* shows the mean SLED with $\pm 1\sigma$ standard deviation from Harrington et al. (2021). The *connected red plus points* show the SLED from the stacked spectrum (Section 6), and this is consistent with the mean SLED of *Planck*-selected DSFGs. We note that several sources appear to exceed the maximum (i.e. thermalized) line ratio profile, and we discuss the implications of this in Section 5.

use error-propagation rules to obtain the total error of each data point. The *dashed black line* at $r_{J_a,J_b} = 1$ indicates the constant-brightness or thermalized profile ($I_{CO} \propto J_{up}^2$), typically assumed to be the maximum excitation SLED of a galaxy.

Similar to Fig. 2, the majority of sources fall within the mean SLED from Harrington et al. (2021) (*grey filled region*). A handful of sources already appear to peak at or lower than $J_{up} = 3$, with the majority of sources showing a peak in their CO SLED between $J_{up} = 4$ and 6 or beyond. Several sources, however, lie on the *unexpected* side of the thermalization curve, indicating super-thermal excitation within our sources (see Section 5). We note that there is a strong redshift dependence for what lines are detected for each source. This is due to the fixed spectral windows in the ALMA observations described in Urquhart et al. (2022), where sources at higher redshifts had higher-J CO lines redshifted into the observing windows.

4.2 Spectral line comparison

In this subsection, we compare several spectral lines against the bolometric infrared luminosity (8–1000 μm) for the BEARS galaxies. We choose to derive the infrared luminosity using only the 151 GHz flux density from the Band 4 observations with ALMA, since all galaxies are identified through their 151 GHz flux density, and over half of all sources discussed in this paper (40 out of 71) have multiples that make direct comparison to the *Herschel* and SCUBA-2 photometry unreliable. For all sources in our sample, the observed

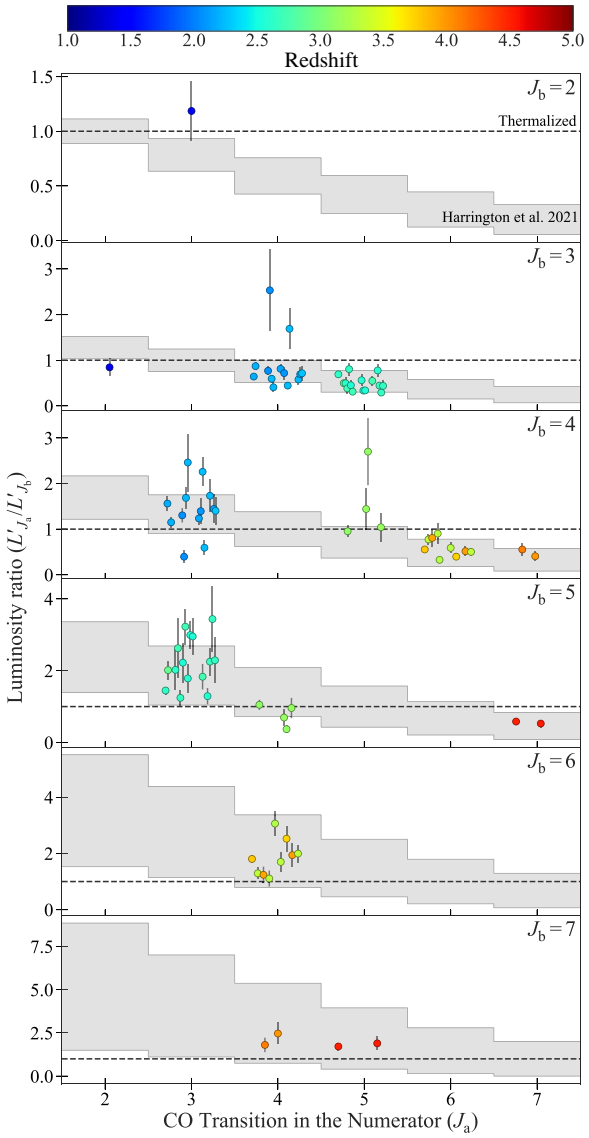

Figure 3. Line luminosity ratios between the different lines plotted against the CO transition in the denominator (i.e. the *normalizing* CO line transition) using equation (2). We compare the ratios to the expected ratios of the compilation of Harrington et al. (2021) (*grey filled region*), and the constant brightness profile (*flat dashed line*). The colour of the data markers reflects their redshift (*blue to red* equalling *low to high redshift*). *Each panel* indicates a different CO-transition in the denominator of the luminosity ratio, while the *x-axis* refers to the CO transition in the numerator. We manually shift the points between $J_a - 0.5$ and $J_a + 0.5$ so as not to overlap. The constant brightness profile assumes equal excitation among all CO transitions, and thus has a uniform value of 1.0 for all CO transitions. The lines detected for each source depends strongly on their spectroscopic redshift, and is reflected in the clustering of colours at specific CO line transitions. For non-thermalized CO lines, the points lie above 1 at x-values lower than J_b, and below 1 at x-values larger than J_b.

151 GHz emission probes the infrared emission, as all sources lie beyond $z > 1$. Although Bendo et al. (2023) provide estimates of the photometric properties of individual sources and sources with multiples at the same confirmed redshift, a comprehensive study across our sample is still elusive, as it requires extensive work using deblending techniques on the *Herschel* and SCUBA-2 photometry for sources with multiples. The scope of this paper is to provide a

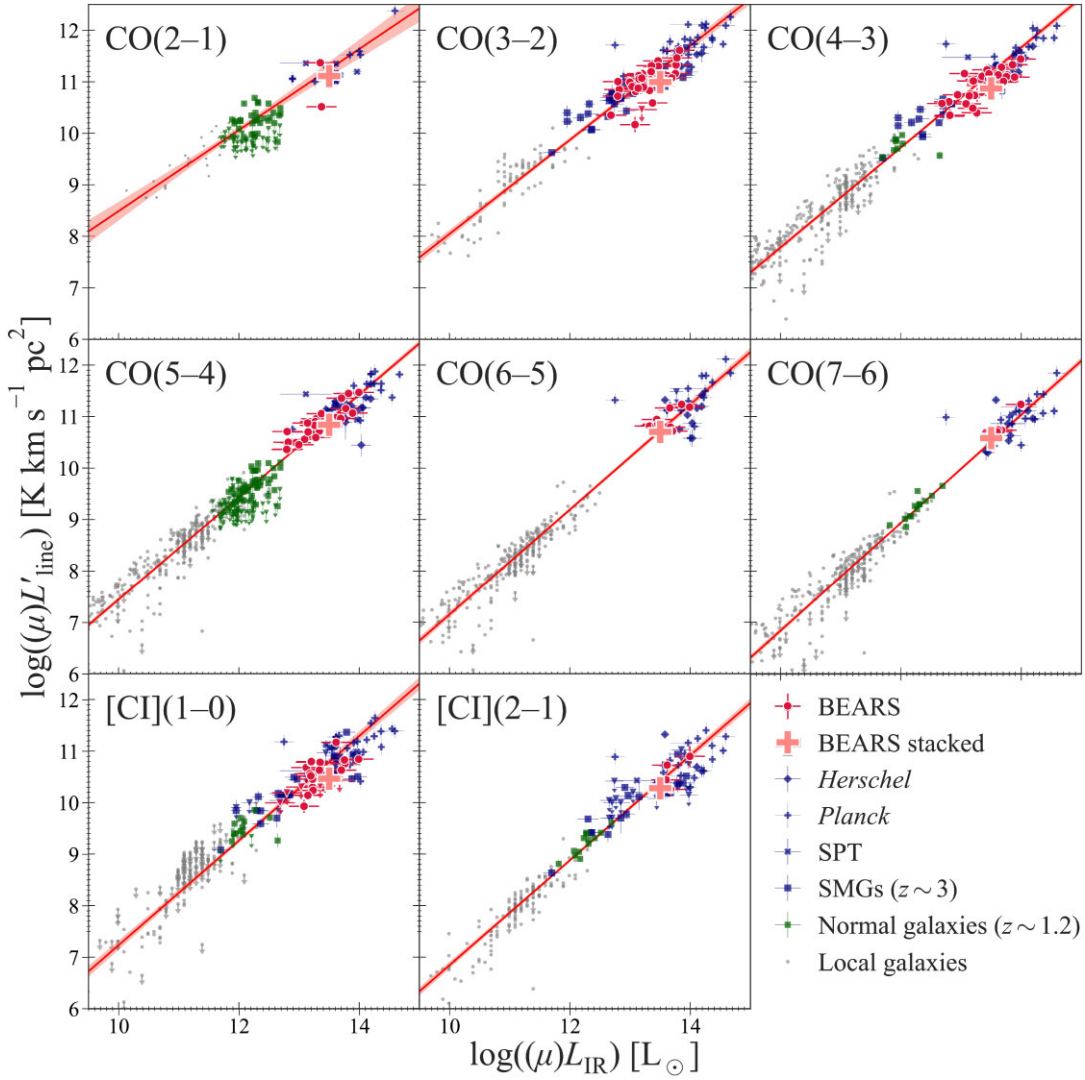

Figure 4. Detected CO and [C I] emission lines versus the infrared luminosity. We compare the line luminosity of the BEARS sources against reference samples of low-redshift star-forming galaxies, including infrared-luminous galaxies (Greve et al. 2014; Liu et al. 2015; Rosenberg et al. 2015; Kamenetzky et al. 2016; Yang et al. 2017; *grey points*), high-redshift star-forming galaxies (Valentino et al. 2020a; *green squares*), and DSFGs (Walter et al. 2011; Alaghband-Zadeh et al. 2013; Bothwell et al. 2017; Yang et al. 2017; Harrington et al. 2021; *blue squares, diamonds, crosses, and plus points*). We use a linear-regression-fitting technique to estimate the scaling relations, accounting for errors in both the line and infrared luminosities. The red solid line and background pink shade mean the best-fitting result and $\pm 2\sigma$ uncertainty. The best-fitting parameters of the scaling relations are reported in Table B1. The *large plus sign* indicates the result from the stacked spectrum (see Section 6). Our sources, as well as the stacked result, are consistent with previous works.

comprehensive study of the gas properties of our sample, and we therefore take a simplified approach using the single data point all our sources share (i.e. the 151 GHz detection) and leave a deblending study for future work. The infrared luminosity is calculated assuming an MBB with an average dust temperature of 35 K and a dust-emissivity index (β) of 2. This is in line with the photometric study of individual sources and sources with multiples at the same redshifts from Bendo et al. (2023), which finds an average dust temperature of 32.3 ± 5.5 and a β of 2.00 ± 0.35, and also agrees with previous studies of dusty galaxies in the distant Universe (e.g. Eales et al. 2000; Dunne & Eales 2001). A single-temperature MBB is the most basic representation of the emission of a dusty galaxy, and allows for an easy comparison or future translation to other studies, unlike a direct fit to an observed spectrum such as the Cosmic Eyelash (e.g. Ivison et al. 2010; Swinbank et al. 2010). The 151 GHz emission traces the Rayleigh–Jeans tail of the emission, and we are thus sensitive to the larger but colder reservoirs of dust. However, we note that this data point provides little constraint on any warmer dust that could be present inside a small portion of these galaxies. We account for the CMB using the appropriate equations from da Cunha et al. (2013), which correct both for the dust emission in contrast to the CMB, as well as additional dust heating by the CMB. For single-component sources, we validate our method against the luminosities from Bakx et al. (2020b) and Bendo et al. (2023), and find similar infrared luminosities within the typical uncertainty of the 151 GHz flux density. Throughout this paper, we calculate the SFR assuming the Kennicutt & Evans (2012) relation of SFR $[M_\odot\ yr^{-1}] = 1.47 \times 10^{-10} L_{IR}\ [L_\odot]$.

Fig. 4 shows the line luminosity of the CO and [C I] lines against the infrared luminosity of the BEARS sources. These sources are compared against the relationships for low- (Greve et al. 2014; Liu et al. 2015; Rosenberg et al. 2015; Kamenetzky et al. 2016;

Yang et al. 2017) and high-redshift (Walter et al. 2011; Alaghband-Zadeh et al. 2013; Bothwell et al. 2017; Yang et al. 2017; Valentino et al. 2020a; Harrington et al. 2021) galaxies. In order to estimate the scaling relations accounting for errors in both the line and infrared luminosity, we use a linear regression fitting technique of SCIPY (Virtanen et al. 2020) ODR (orthogonal distance regression) package, which is an implementation of the FORTRAN ODRPACK package (Boggs et al. 1992). The best-fitting parameters in the scaling relations are reported in Table B1 according to the perscription

$$\log_{10}\left(L'_{\rm line}\ \left[{\rm K\ km\ s^{-1}\ pc^2}\right]\right) = a\log_{10}\left(L_{\rm IR}\ [{\rm L_\odot}]\right) + b. \quad (3)$$

The line luminosity scalings of BEARS galaxies are consistent with the reference samples, spanning over four orders of magnitude for all lines. The best-fitting results of the CO and [C I] lines (except CO (2–1) and perhaps CO (3–2)) agree with a linear scaling relation across our sample. While the line fits are well constrained, the source-to-source variation across the reference samples and our data are of the order of ±0.5 dex. This means that we can convert the luminosities of these emission lines into SFR estimates.

4.3 Inferred Schmidt–Kennicutt relation of *Herschel* sources

Fig. 5 shows the SK scaling relation – star formation surface density against molecular gas mass surface density (Schmidt 1959; Kennicutt 1989) – for all 71 BEARS sources detected in either [C I] or CO. The molecular hydrogen mass in the galaxy is calculated using

$$M_{\rm H_2} = \alpha L'_{\rm line}. \quad (4)$$

When available, we use the [C I] ($^3P_1$–$^3P_0$) line to calculate the molecular gas mass, otherwise we use the mean line luminosity ratios obtained from the turbulence model in Harrington et al. (2021) to calculate the CO (1–0) line luminosity, specifically $r_{2,1} = 0.88 \pm 0.07$, $r_{3,1} = 0.69 \pm 0.12$, $r_{4,1} = 0.52 \pm 0.14$, and $r_{5,1} = 0.37 \pm 0.15$. We use each conversion factor from the recent study of Dunne et al. (2021, 2022):

$$\alpha_{\rm [CI]} = 17.0\ \left[{\rm M_\odot}\ \left({\rm K\ km\ s^{-1}\ pc^2}\right)^{-1}\right], \quad (5)$$

$$\alpha_{\rm CO} = 4.0\ \left[{\rm M_\odot}\ \left({\rm K\ km\ s^{-1}\ pc^2}\right)^{-1}\right]. \quad (6)$$

They estimate this value through a self-consistent cross-calibration between three important gas-mass tracers (i.e. [C I], CO and submm dust continuum). In total, they use 407 galaxies from low to high-redshift ($z \approx 6$), and fail to find any evidence for a bimodality in the gas conversion factors between different galaxy types. As a sanity check, our sources also have a good agreement in their estimates of the molecular gas mass between [C I] and CO. The $\alpha_{\rm CO} = 4.0\ {\rm M_\odot}\ ({\rm K\ km\ s^{-1}\ pc^2})^{-1}$ value includes the additional helium correction (see Bolatto, Wolfire & Leroy 2013 for a review) of 1.36. This $\alpha_{\rm CO}$ value is larger than the typically assumed 0.8 for star-bursting galaxies (see e.g. Casey et al. 2014); however, this is in line with recent studies of *Planck*-selected galaxies (Harrington et al. 2021). We note that the lower $\alpha_{\rm CO}$ values from previous studies are better able to align the observed dynamical and molecular gas masses (see Section 4.5). We use the deconvolved `IMFIT` result discussed in Section 4.4 to estimate the surface densities, where *circles* indicate sources with size estimates and *circles with diagonal arrows* indicate sources with upper limits on their size estimates. We use the same (continuum) size estimate for both the molecular gas and star formation surface densities. These are compared against reference samples at low- (Kennicutt 1989; de los Reyes & Kennicutt 2019a, b; Kennicutt & De Los Reyes 2021) and high-redshift (Tacconi et al. 2013; Hatsukade et al. 2015; Chen et al. 2017, and references therein).

We adjust the reference sample of DSFGs (*blue squares*) from Chen et al. (2017, and references therein) from the initially assumed $\alpha_{\rm CO} = 0.8$ to 4.0 for a fair comparison, where the *black arrow* in the top left part of the graph indicates the effect of this change in $\alpha_{\rm CO}$. Recent studies have shown that the size of the molecular gas reservoir extends beyond the bright star-forming region (e.g. Chen et al. 2017). Therefore, the arrow can also be used to indicate the effect of a 2.2 times ($= \sqrt{4/0.8}$) larger radius of the molecular reservoir relative to the star-forming region. The diagonal dashed lines indicate the depletion time-scales of 1 Myr to 10 Gyr, defined as the molecular gas mass divided by the SFR ($t_{\rm dep} = \mu M_{\rm mol}/\mu{\rm SFR}$).

The BEARS sources appear to have shorter depletion times than local spirals and dwarf galaxies, as well as $z \approx$ 1–3 star-forming galaxies, suggesting accelerated star formation in these systems and hence implying that these systems are not simply scaled-up versions of gas-rich, normal star-forming systems (Cibinel et al. 2017; Kaasinen et al. 2020). The BEARS sources have, on average, longer depletion times than the DSFGs from Hatsukade et al. (2015) and Chen et al. (2017, and references therein). Harrington et al. (2021) also report the longer depletion time-scale for *Planck*-selected DSFGs, suggesting that DSFGs are not necessarily consuming their gas faster than other active galaxies. However, they do appear to have a similar slope that is of the order of unity or slightly steeper. This is in contrast to the slopes reported in early studies (e.g. 1.25–1.44 by Gao & Solomon 2004) and in agreement with current studies (e.g. 0.9–1.4 by Tacconi et al. 2013, 2018; Tacconi, Genzel & Sternberg 2020 and 1.13 by Wang et al. 2022). There exists, however, an ambiguity in the measured sizes of these kind of studies. As noted in Chen et al. (2017), if the dust size is used instead of the CO-based size estimate, the gas surface density of the sources could increase by over an order of magnitude. High-resolution imaging of DSFGs have shown these sources to be compact dusty systems (e.g. Ikarashi et al. 2015; Barro et al. 2016; Hodge et al. 2016; Gullberg et al. 2019; Pantoni et al. 2021) with sizes of the order of a single kiloparsec. Instead, relative to the $z \sim$ 2–4 SMGs, the BEARS systems are likely hosting more extended star formation in their systems seen through an increase in their depletion time-scales. Here, we note an intrinsic bias in our sample, since all galaxies have spectroscopic redshifts based on CO line measurements. Low gas-surface-density galaxies might remain without a spectroscopic redshift, which could bias our sample towards higher gas surface densities.

The size estimates from `IMFIT` are of the same order as the beam size of the current ALMA observations (≈ 2 arcsec), and could be affected by the magnification of gravitational lensing. These effects, however, would only move the data points along the *diagonal lines* of constant depletion time-scales (if we exclude differential lensing), and would not affect our estimates of the SK-slope; however, it is difficult to exclude any effects from differential lensing at the current resolution (Serjeant 2012).

4.4 Dynamical properties of BEARS galaxies

The moderate resolution of our observations (≈ 2arcsec) and velocity width of the lines provides a potential window on the dynamical nature of these high-redshift galaxies. We calculate (apparent) dynamical virial and rotational mass following earlier studies (Neri et al. 2003; Tacconi et al. 2006; Bouché et al. 2007; Engel et al. 2010; Bothwell et al. 2013; Bussmann et al. 2013; Wang et al. 2013; Willott, Bergeron & Omont 2015; Venemans et al. 2016; Yang et al. 2017) as

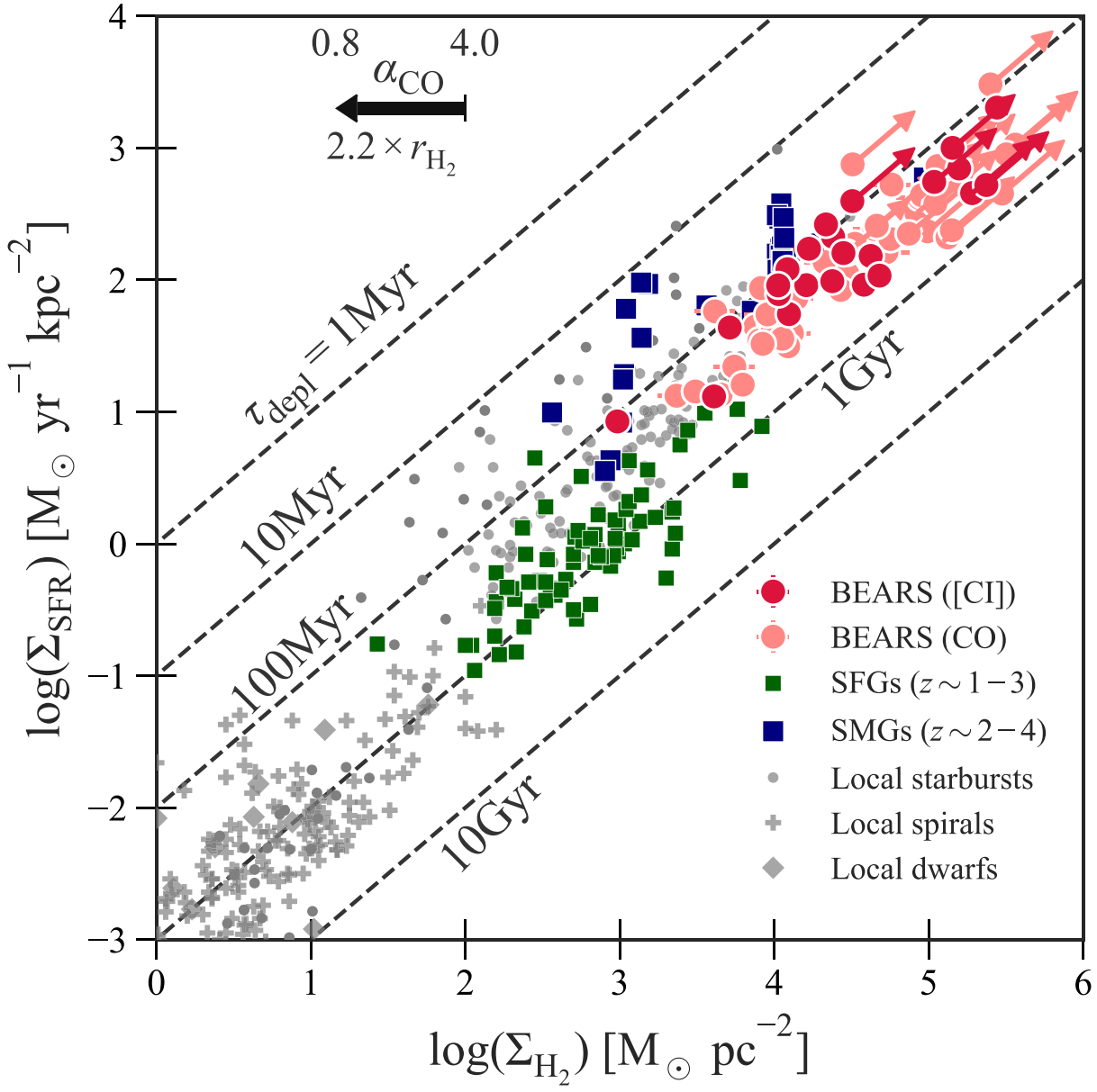

Figure 5. SK scaling relation, i.e. star formation surface density against molecular gas mass surface density (Schmidt 1959; Kennicutt 1989) for the BEARS galaxies detected either in [C I] (*red*) or CO (*light red*). We use the deconvolved IMFIT result discussed in Section 4.4 to estimate the surface densities, where *circles* indicate sources with size estimates and *circles with diagonal arrows* indicate sources with upper limits on their size estimates. They are compared against reference samples of low-redshift galaxies (Kennicutt 1989; de los Reyes & Kennicutt 2019a, b; Kennicutt & De Los Reyes 2021; *grey points, plus points, and diamonds*), high-redshift star-forming galaxies (Tacconi et al. 2013; *green squares*), and high-redshift DSFGs (Hatsukade et al. 2015; Chen et al. 2017 and references therein; *blue squares*). We use an $\alpha_{[CI]}$ value of 17.0 and an α_{CO} value of 4.0 from the recent study of Dunne et al. (2021, 2022). We adjust the reference sample of DSFGs (*blue squares*) from Chen et al. (2017) from the initially assumed $\alpha_{CO} = 0.8$ to 4.0 for a fair comparison, where the *black arrow* in the top left part of the graph indicates the effect of this change in α_{CO}. Recent studies have shown that the size of the molecular gas reservoir extends beyond that of the bright star-forming region. The arrow can thus also be used to indicate the effect of a 2.2 times larger radius of the molecular reservoir relative to the star formation region. The *diagonal dashed lines* indicate the depletion time-scales of 1 Myr to 10 Gyr. The BEARS sources appear to have slightly longer gas depletion times than DSFGs from Chen et al. (2017, and references therein); however, they do appear to have a similar slope. The SK slope for the BEARS sample is approximately unity.

$$M_{\rm dyn,vir} = 1.56 \times 10^6 \left(\frac{\sigma}{\rm km\ s^{-1}}\right)^2 \left(\frac{r}{\rm kpc}\right) {\rm M}_\odot, \quad (7)$$

$$M_{\rm dyn,rot} = 2.32 \times 10^5 \left(\frac{v_{\rm circ}}{\rm km\ s^{-1}}\right)^2 \left(\frac{r}{\rm kpc}\right) {\rm M}_\odot, \quad (8)$$

in which $\sigma = \Delta V_{CO}/(2\sqrt{2\ln 2})$, ΔV_{CO} is the FWHM of the line, $v_{\rm circ}$ is the circular velocity (using $v_{\rm circ} = 0.75\Delta V_{CO}/\sin i$, with the inclination angle set as the average of $i = 55$ deg following Wang et al. 2013), and r is the effective radius. Here, we note that a wrong estimate of i may lead to a significant systematic shift

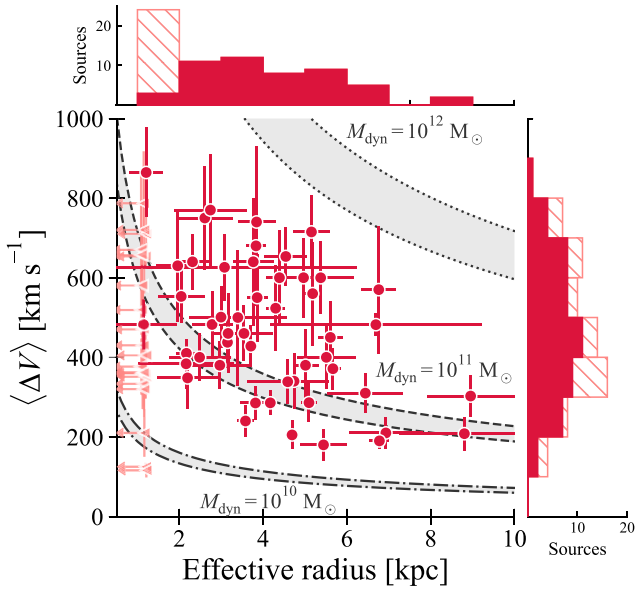

Figure 6. Velocity widths versus effective radii for sources with detected line emission. *Dash–dotted, dashed, and dotted lines* show constant dynamical masses, which are 10^{10}, 10^{11}, and 10^{12} M$_\odot$, respectively. *Grey shaded regions* are the variations in which equations of rotational (upper) or virial (lower) estimates shown in Yang et al. (2017) (i.e. equations 7 and 8) are selected to calculate dynamical mass. The *pink data points* represent the upper limits of the size estimation from IMFIT. These sources are unresolved so we set the size of them to the minimum size of detected sources (*red points*). We show the histograms of the velocity and radius distributions on the right and top sides of the graph, respectively; the *red filled and pink hatched histograms* correspond to the data points with the same colour.

for individual objects, but that using the average value is useful for statistical estimates of $M_{\rm dyn}$ across the population, even though individual $M_{\rm dyn}$ estimates are not necessarily reliable. We calculate the effective radius from the Band 4 continuum image using the CASA tool IMFIT. Here, we note that the size estimation from Band 4 continuum might not equal the source size probed by the CO emission lines (e.g. Chen et al. 2017). The source size is calculated from the deconvolved major and minor axes, added in quadrature. Any measurement errors are also added in quadrature.

In Fig. 6, we show the velocity width distribution of the sources as a function of their effective radius. 21 galaxies do not have reliable source sizes from the IMFIT routine, and are shown in *light red*. For these 21 galaxies, we set their sizes to 0.14 arcsec, the lower end of the reliable IMFIT size estimates. There are three likely interpretations of these source sizes. The first and most straightforward is that the source is unlensed, and therefore that the sizes represent the physical sizes of the galaxies. The second option is that the sources are strongly gravitationally lensed, and that the spatial extent is that of a single gravitationally lensed arc resulting from a foreground galaxy cluster or group. In that case, the observed angular size in the tangential direction would be the magnification μ multiplied by the intrinsic size, while in the radial direction there would be no magnification. The third option is that the system is a galaxy–galaxy gravitational lens system, in which case the angular extent is likely to reflect that of the Einstein radius of the lensing geometry rather than the size of the BEARS galaxy.

We compare the effective radii and velocities with fixed-mass solutions to the dynamical mass equations, on the simplest assumption that the systems are unlensed. Most galaxies have dynamical masses between 10^{11} and 10^{12} M$_\odot$, and the variation is only minor between rotational (upper) and virial (lower) mass limits. There are several caveats to this method, however. First, we do not have any direct reason to assume that these systems are either virialized or stably rotating. Secondly, the systems may be gravitational lenses, in which case the radii in equations (7) and (8) are overestimates of the underlying source sizes.

These (apparent) dynamical galaxy masses are at the most massive end of the star formation main sequence, and appear to indicate that these systems are some of the most massive galaxies in the Universe. Indeed, DSFGs have often been suggested as progenitors of red-and-dead giant elliptical galaxies at $z = 0$ (Swinbank et al. 2006; Coppin et al. 2008; Toft et al. 2014; Ikarashi et al. 2015; Simpson et al. 2017; Stach et al. 2017) given (1) their high stellar masses (Hainline et al. 2011; Aravena et al. 2016), (2) their high specific SFRs (Straatman et al. 2014; Spilker et al. 2016; Glazebrook et al. 2017; Schreiber et al. 2018; Merlin et al. 2019), and (3) their location in overdense regions (Blain et al. 2004; Weiß et al. 2009; Hickox et al. 2012).

However, there exist some important additional caveats to the dynamical mass estimates. A critical underlying assumption is that the systems are self-gravitating and relaxed, as discussed in Dunne et al. (2022). If submm galaxies are dynamically complex, for example if their gas kinematics is dominated by a major merger, then this could yield apparent anomalously large dynamical masses. Dunne et al. (2022) show that a very wide range of star-forming galaxies can be interpreted consistently as having a constant gas mass conversion factor of $\alpha_{\rm CO} = 4.0$ M$_\odot$ (K km s^{-1} pc^2)$^{-1}$, and attribute the previous roughly 5 times lower estimates to the unrelaxed dynamical states of submm galaxies (e.g. their equation 9). On the contrary, galaxies undergoing rapid collapse triggering bursts of star formation through violent disc instabilities – as for example seen in SDP.81 (Dye et al. 2018) – could cause us to underestimate the dynamical masses. Similarly, differential lensing (Serjeant 2012) of low-dispersion star-forming regions could cause us to underestimate the total velocity widths and thus the dynamical masses.

4.5 Molecular gas mass

Fig. 7 shows the (apparent) dynamical virial mass of each galaxy against the estimated molecular gas mass, on the assumptions of no gravitational lensing (see above) and dynamically relaxed (i.e. no major merging) states in the submm galaxies. The figure also shows the 1:4, 1:1, and 4:1 scaling relations between the molecular and dynamical masses. Remarkably, the majority of our galaxies have a molecular gas mass above that of the dynamical mass. We find a scatter of half an order of magnitude around the 4:1 scaling relation, with galaxies having large velocity widths (ΔV) scattering towards higher dynamical masses and vice versa.

Gravitational lensing does not resolve this apparently unphysical pair of mass constraints. Lens magnification corrections would reduce $M_{\rm gas}$ estimates, because this scales with the line luminosity, but lensing would also reduce $M_{\rm dyn}$. The latter correction may even be stronger than that for $M_{\rm gas}$, especially if the physical size estimates from our marginally resolved ALMA data in equations (7) and (8) are dominated by Einstein radii, however, the positions of galaxies above the 'main sequence' in the SK plane in Fig. 5 would be insensitive to magnification effects.

An alternative reading of this apparently unphysical result in Fig. 7 is that the underlying assumption of the dynamical mass estimates is false, i.e. that the systems are not dynamically relaxed (e.g. Dye et al. 2018) or that the line velocity does not represent the bulk of

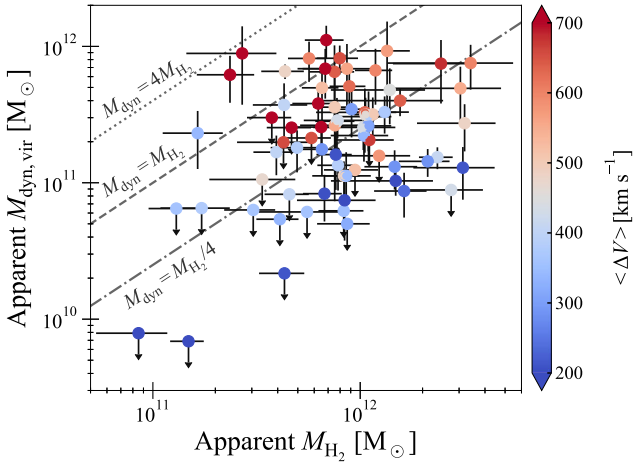

Figure 7. Comparison of the molecular gas masses to dynamical masses for the BEARS sources. The colours indicate the average velocity width of the emission lines, and upper limits indicate sources without accurate size estimates from the IMFIT analysis. The majority of sources lie below the $M_{\rm dyn} = M_{\rm gas}$ relation (*dashed line*), suggesting that we may be underestimating the dynamical masses of these systems. This can be caused by gravitational lensing, which boosts the observed gas mass, or by the compact nature of the dust emission.

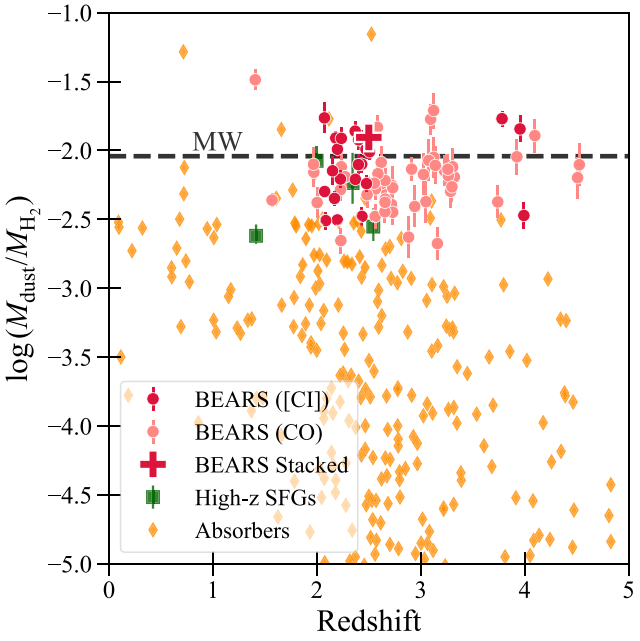

Figure 8. Redshift evolution of dust-to-gas ratio of our galaxies, as well as high-redshift star-forming galaxies from Shapley et al. (2020) (*green squares*), and damped Lyman-α absorber systems from De Cia et al. (2018) and Péroux & Howk (2020, and references therein) (*orange points*). The lack of redshift evolution and low scatter across all redshifts suggests we are witnessing an approximately single galaxy type with (recent) intense star formation in line with a metallicity of close to the Milky Way ($\approx 0.45 Z_\odot$; Draine & Li 2007a; Draine et al. 2014).

the galaxy (e.g. Hezaveh, Marrone & Holder 2012; Serjeant 2012). We argue therefore that our results may still be consistent with the interpretation of a constant $\alpha_{\rm CO}$ conversion factor, in agreement with the merger hypothesis for submm galaxies (Sanders et al. 1988; Hopkins et al. 2008).

Nevertheless, the gas mass alone (modulo the gas fraction) indicates that these systems are at the massive end of the galaxy mass function. The discovery of massive, quenched systems around the first billion years of the Universe (Straatman et al. 2014; Glazebrook et al. 2017; Schreiber et al. 2018) indicates the need for galaxies that rapidly build-up mass and, more importantly, rapidly quench afterwards. At gas masses over 10^{11} $M_\odot$, DSFGs are likely progenitors of the quenched population, although the quenching time-scale of 0.1–1 Gyr from Fig. 5 does not appear to be rapid enough to quench the systems adequately.

4.6 Dust-to-gas mass ratio

The dust-to-gas mass ratio is the dust mass divided by the molecular gas mass, and as the dust locks up metals produced through bursts of star-formation, this ratio forms an important evolutionary probe across time (Péroux & Howk 2020; Zabel et al. 2022) sensitive to the gas-phase metallicity in a system (James et al. 2002; Draine & Li 2007; Galliano, Dwek & Chanial 2008; Leroy et al. 2011; Rémy-Ruyer et al. 2014; Shapley et al. 2020; Granato et al. 2021). Meanwhile, the dust destruction mechanisms require the conditions for dust formation to be recent ($\sim$ 0.3–0.5Gyr, Hou et al. 2019; Hu et al. 2019; Osman, Bekki & Cortese 2020). Models further suggest that these high SFRs also correlate with in/outflows (Triani et al. 2020, 2021), ubiquitously observed for DSFGs (Spilker et al. 2020a, b; Berta et al. 2021; Butler et al. 2021; Riechers et al. 2021).

Fig. 8 shows the dust-to-gas ratio for the BEARS targets, as well as for other high-redshift star-forming galaxies from Shapley et al. (2020) and damped Lyman-α absorber systems from De Cia et al. (2018) and Péroux & Howk (2020, and references therein). We use the 151 GHz flux density from Bendo et al. (2023), and convert this to a dust mass assuming $S_\nu = \kappa_\nu B_\nu(T = 35\ {\rm K}) M_{\rm dust} D_{\rm L}^{-2}$, where κ_ν is the dust mass absorption coefficient, B_ν is the Planck function at temperature $T = 35$ K, and $D_{\rm L}$ is the luminosity distance. Here, we assume a $\beta = 2$, and approximate the dust mass absorption coefficient (κ_ν) as $\kappa_\star(\nu/\nu_\star)^\beta$, with ($\kappa_\star$, $\nu_\star$) as (10.41 cm^2 g^{-1}, 1900 GHz) from Draine (2003). The BEARS sources have ratios of the order 10^{-2} to 10^{-3}, similar to what is seen in local dusty galaxies and high-redshift DSFGs. Absorber systems are typically selected solely by their bulk atomic gas and are thus sensitive to the metallicity-evolution of galaxies across time. Unlike absorber systems, BEARS and other SFGs (Shapley et al. 2020) do not show any redshift evolution, in agreement with a metallicity close to the Milky Way (Draine & Li 2007a; Draine et al. 2014). The low scatter and lack of trend with redshift suggests that we are witnessing a single star-forming phase, and the high dust-to-gas ratio suggests that this phase occurred relatively recently.

4.7 Photodissociation regions inside DSFGs

Fig. 9 shows the luminosity ratio of [C I] ($^3P_1$–$^3P_0$) to CO (4–3) (*left-hand panel*) and [C I] ($^3P_2$–$^3P_1$) to CO (7–6) (*right-hand panel*) against their respective [C I] luminosity over infrared luminosity. In total, 19 BEARS sources have both [C I] ($^3P_1$–$^3P_0$) and CO (4–3) observations, and four BEARS sources have [C I] ($^3P_2$–$^3P_1$) and CO (7–6) observations. Here, we calculate the line luminosity using the typical equation from Solomon et al. (1997),

$$L = 1.04 \times 10^{-3} S \Delta v f_{\rm obs} D_{\rm L}^2\ [{\rm L}_\odot]. \quad (9)$$

We also include the reference samples of local U/LIRGs (Michiyama et al. 2021 in the left-hand panel and Lu et al. 2017 in the right-hand

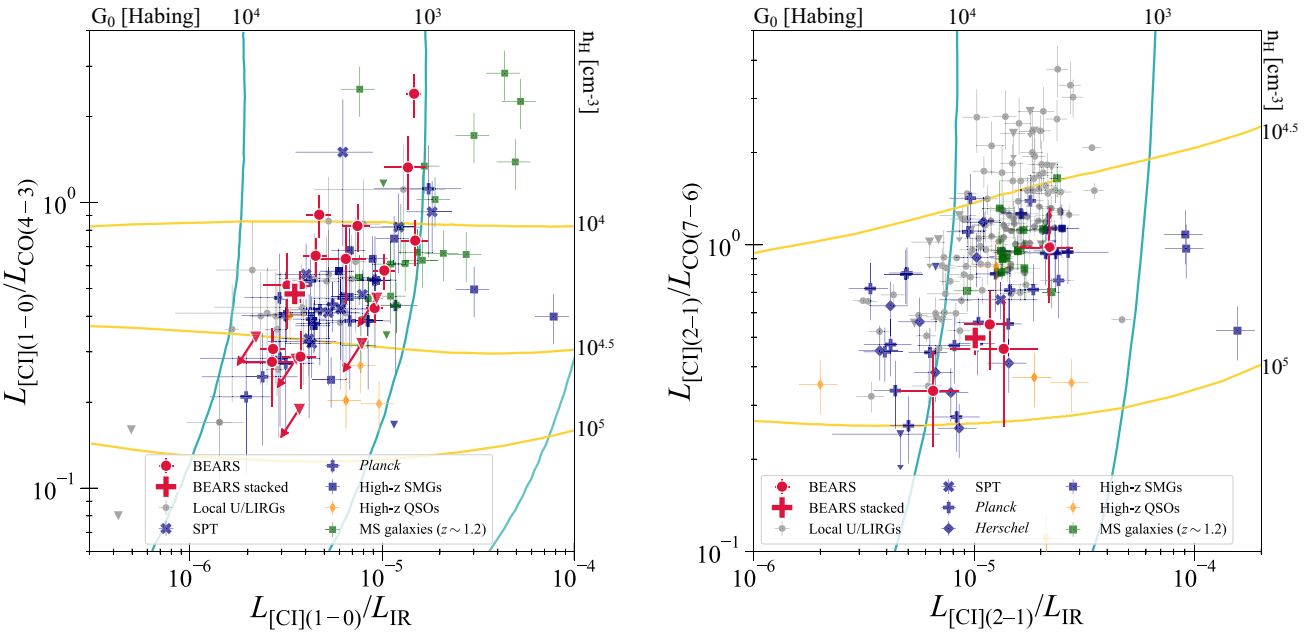

Figure 9. *Left-hand panel*: Ratio of [C I] ($^3P_1$–$^3P_0$) to CO (4–3) plotted versus [C I] ($^3P_1$–$^3P_0$) luminosity over infrared luminosity for 19 BEARS sources with both [C I] ($^3P_1$–$^3P_0$) and CO (4–3) observations (*red circles and downward triangles* for detections and upper limits, respectively) as well as reference samples of local U/LIRGs (Michiyama et al. 2021; *grey points*), high-redshift SPT-sources (Bothwell et al. 2017; *blue crosses*) and *Planck*-sources (Harrington et al. 2021: *blue plus points*), classical SMGs (*blue squares*), QSOs at $z \simeq$ 2–4 (*orange diamonds*), and main-sequence galaxies at $z \simeq 1.2$ (*green squares*) from Valentino et al. (2020b, and references therein). We also include the result from stacking (*red plus sign*). *Right-hand panel*: Ratio of [C I] ($^3P_2$–$^3P_1$) to CO (7–6) plotted versus [C I] ($^3P_2$–$^3P_1$) luminosity over infrared luminosity for four BEARS sources with both [C I] ($^3P_2$–$^3P_1$) and CO (7–6) observations (*red circles* for detections) as well as reference samples of local U/LIRGs (Lu et al. 2017; *grey points*), high-redshift SPT-sources (Jarugula et al. 2021; *blue crosses*) and *Planck*-sources (Harrington et al. 2021: *blue plus points*), *Herschel* DSFGs (*blue diamonds*), classical SMGs (*blue squares*), QSOs at $z \simeq$ 2–4 (*orange diamonds*) from Valentino et al. (2020b, and references therein), and main-sequence galaxies at $z \simeq 1.2$ (*green squares*) from Valentino et al. (2020a). We also include the result from stacking (*red plus sign*). The PDR models of Kaufman, Wolfire & Hollenbach (2006) are overplotted in both panels, showing the theoretical relations for constant hydrogen densities (*near-horizontal yellow solid lines*) and FUV radiation intensity fields (*near-vertical cyan solid lines*).

panel), DSFGs and Quasi-Stellar Objects (QSOs) in the range of redshift 2–4, main-sequence (MS) galaxies at $z \simeq 1.2$ (Valentino et al. 2020a, b, and references therein), high-redshift SPT sources (Bothwell et al. 2017 in the left-hand panel and Jarugula et al. 2021 in the right-hand panel) and *Planck* sources (Harrington et al. 2021). In this plane, the physical conditions of PDRs (e.g. Hollenbach & Tielens 1999) can be constrained (e.g. Umehata et al. 2020; Valentino et al. 2020b; Michiyama et al. 2021). We investigate the differences in PDR conditions among our and reference samples using `PDRToolbox`[2] (Kaufman et al. 2006; Pound & Wolfire 2008, 2011), which provides the line intensities for each combination of hydrogen density ($n_{\rm H}$) and far-ultraviolet (FUV) radiation intensity fields ($G_0 = 1.6 \times 10^{-3}$ erg s^{-1} cm^{-2}; Habing 1968 units, i.e. the incident FUV field between 6 eV $< h\nu <$ 13.6 eV) assuming plane parallel model originally by Kaufman et al. (1999). We show the theoretical tracks for constant $n_{\rm H}$ and G_0 using *yellow* and *cyan solid lines* in Fig. 9.

Most of our sources are located within $10^4 \leq n_{\rm H} \leq 10^5$ [cm^{-3}] and $10^3 \leq G_0 \leq 10^4$ [Habing]. Our sources exhibit denser and more intense radiation environments than MS galaxies at $z \simeq 1.2$, but similar properties to local U/LIRGs and other DSFGs. This is consistent with previous works (Valentino et al. 2020b; Michiyama et al. 2021), with the exception of the sources HerBS-90 and -131B, where $L_{\rm [CI](1\text{-}0)}/L_{\rm CO(4\text{-}3)} \geq 1$. This suggests that the gas in these two sources is more diffuse, similar to MS galaxies, in line with photoionization modelling to dwarf galaxies by Madden et al. (2020). We note that the offset could also be caused by the different observed line profiles between CO and [C I], i.e. the larger estimation of ΔV in [C I] line emission might have resulted in an overestimate of the line luminosity.

The ISM properties derived from the different atomic carbon lines, [C I] ($^3P_1$–$^3P_0$) and [C I] ($^3P_2$–$^3P_1$), vary slightly in the derived gas densities and FUV intensity fields. This could be due to a change in the internal properties of DSFGs in the early Universe or due to observational biases in selecting our distant galaxies. The observational biases could result from a selection towards higher redshift, since all galaxies with CO (7–6) and [C I] ($^3P_2$–$^3P_1$) are detected at higher redshift, where the lines shift into more favourable parts of the atmospheric windows (and the spectral windows used in Urquhart et al. 2022). More observations are needed to conclusively test the modest discrepancy between the ISM properties derived from the different atomic carbon lines.

We use the PDR model from Kaufman et al. (1999) that supposes the simple 1D geometry assuming three discrete layers, i.e. the [C I] emission comes only from the thin layer between two gas components traced by CO and singly ionized carbon emission ([C II]). Meanwhile, spatially resolved observations of local giant molecular clouds (e.g. Ojha et al. 2001; Ikeda et al. 2002) and active star-forming region in local galaxies (e.g. Israel, Rosenberg & van der Werf 2015) suggest that the CO- and [C I]-bright gas are well mixed. This gas property has been explained more successfully assuming more complicated gas conditions (clumpy geometry: e.g. Stutzki et al. 1998; Shimajiri

[2]https://dustem.astro.umd.edu/index.html

et al. 2013; mixing within highly turbulent clouds: e.g. Xie, Allen & Langer 1995; Glover et al. 2015; and more complicated 3D geometric models: e.g. Bisbas et al. 2012) or additional excitation origins (cosmic rays, CRs: e.g. Papadopoulos et al. 2004; Papadopoulos, Bisbas & Zhang 2018, shocks: e.g. Lee et al. 2019). However, such models require a lot of observational data that trace multiphase ISM. For example, Bothwell et al. (2017) required multitransitions of CO, [C I], and [C II] lines to constrain gas density and FUV intensity.

In particular, recent works show that CRs can dissociate CO molecules more effectively than FUV radiation in molecular clouds because they are not strongly attenuated by dust (e.g. Bisbas et al. 2017). Highly star-forming environments such as the ones expected in our sample result in a large amount of CRs (as seen in the stacked spectrum in Section 6), which will likely affect the properties of the ISM. Bothwell et al. (2017) compare the gas density and FUV intensity obtained from `PDRToolbox` with those from `3D-PDR` (Bisbas et al. 2012) – a model that includes the effect of CRs – for SPT-selected strongly lensed DSFGs. This is a fair comparison, as SPT-selected DSFGs have similar infrared luminosities as our sample. As a result, they find consistency between the two models for the FUV strength, however, a relatively higher gas density ($\langle \log n_{\rm H} \rangle = 5.2 \pm 0.6$ cm $^{-3}$) compared to the 1D model from Kaufman et al. (1999) ($\langle \log n_{\rm H} \rangle = 4.4 \pm 0.4$ cm $^{-3}$). Since $L_{\rm [CI](1-0)}/L_{\rm CO(4-3)}$ ratio is sensitive to gas density, CRs can cause us to underestimate the gas density of our sources since we do not consider CRs in our current work. At the moment, it is hard to constrain the physical properties through only two emission lines and infrared luminosity, possibly leading us to underestimate the gas density by nearly one order of magnitude (0.8 dex).

4.8 Water lines from BEARS galaxies

Fig. 10 provides a comparison of $L_{\rm IR}$ against the luminosity ratio of H_2O (2_{11}–2_{02}) emission to $L_{\rm IR}$ for five BEARS sources, three of which are not detected above 3σ. We compare the galaxies against reference samples from Yang et al. (2013, 2016), Lu et al. (2017), Apostolovski et al. (2019), Bakx et al. (2020c), Neri et al. (2020), and Jarugula et al. (2021). We confirm tight correlations between them and derive a scaling relation for the H_2O emission using linear regression to all the samples shown in Fig. 10 in order to account for errors in both the infrared luminosity and line emission, minimizing the fit of

$$\log_{10}\left(\frac{L_{\rm H_2O}}{L_{\rm IR}}\right) = a\,\log_{10}\left(L_{\rm IR}[{\rm L}_\odot]\right) + b, \tag{10}$$

where both a and b are left as fitting parameters.

A super-linear relation seems to better fit all the observed data across four orders of magnitude, with $a = 0.12 \pm 0.04$ and $b = -6.8 \pm 0.5$, which is consistent with previous studies (e.g. Omont et al. 2013; Yang et al. 2013, 2016). Our linear regression fitting favours a super-linear relation at the 3σ level, although we note that our observations only add two H $_2$O detections, and three upper limits. Contrary to Jarugula et al. (2021), we also include sources from Lu et al. (2017) that are not included in Yang et al. (2013). The improved fitting constraints from the additional sources since Yang et al. (2016) – who find ($a = 1.16 \pm 0.13$) – likely cause an increase in the significance of the super-linear fit result from ~ 1 to $\sim 3\sigma$.

Both observations (e.g. Riechers et al. 2013; Yang et al. 2013, 2016; Apostolovski et al. 2019; Jarugula et al. 2021) and modelling (e.g. González-Alfonso et al. 2010, 2014) find a strong correlation between the infrared luminosity and the H_2O line emission. The

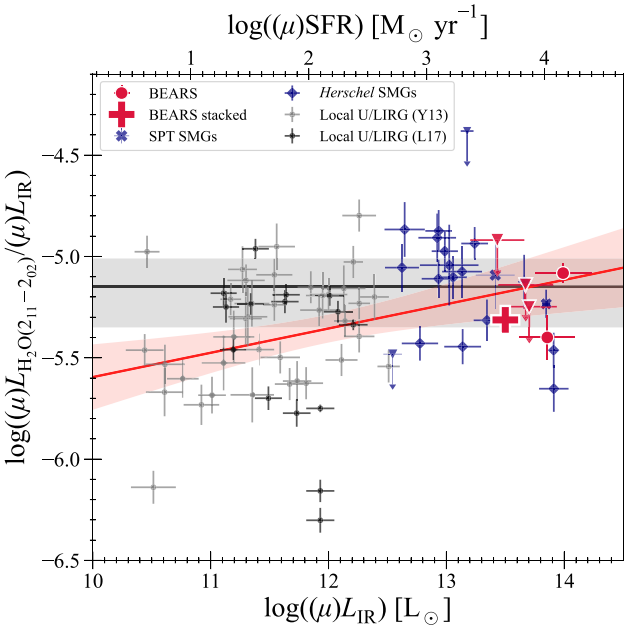

Figure 10. Infrared luminosity plotted against the luminosity ratio of H_2O (2_{11}–2_{02}) emission to $L_{\rm IR}$ of BEARS galaxies (*red circles, downward triangles, and plus point* for detections, upper limits, and stacked spectrum, respectively) is shown against a comparison of local infrared-bright galaxies (*grey points*; Yang et al. 2013, *black points*; Lu et al. 2017), *Herschel*-selected DSFGs (*blue diamonds*; Yang et al. 2016; Bakx et al. 2020c; Neri et al. 2020), and SPT-selected DSFGs (*blue crosses*; Apostolovski et al. 2019; Jarugula et al. 2021). The *red line and filled region* shows the linear regression fit of $\log_{10}\left(L_{\rm H_2O}/L_{\rm IR}\right) = a\log_{10}\left(L_{\rm IR}\right) + b$ with the $\pm 2\sigma$ uncertainty. As a result of fitting, we find $a = 0.12 \pm 0.04$ and $b = -6.8 \pm 0.5$. The *black line and grey filled region* corresponds to the best-fitting result with the slope fixed to zero from Jarugula et al. (2021), where we use a factor of 1.55 to convert from far-infrared luminosity to infrared luminosity and assume the Kennicutt & Evans (2012) relation of SFR $= 1.47 \times 10^{-10} L_{\rm IR}$. Partial collisional excitation of the H_2O line could explain our super-linear fit to the luminosity ratio (González-Alfonso et al. 2022).

moderately higher transitions of H_2O (above ≈ 100 K) are not excited through collisions, but instead infrared pumping is expected to be their dominant excitation mechanism (González-Alfonso et al. 2022). Meanwhile, the $J = 2$ lines are likely still partially collisionally excited, which could explain the super-linear scaling relation (Yang et al. 2013; Liu et al. 2017), although the super-linear trend appears to go away in resolved observations (Yang et al. 2019), and could be due to optical depth effects (González-Alfonso et al. 2022). The origins of our observed super-linear relation will require detailed radiative transfer modelling across multiple water transitions. We briefly note that this result is in contrast to the picture of H $_2$O line luminosity being proportional to SFR, even down to the resolved scale of individual GMCs (e.g. Jarugula et al. 2021).

5 COMPANION SOURCES WITH UNUSUALLY BRIGHT LINES: THE BEARS CUBS

In Section 4.1, we identified four sources with line ratios in excess of the thermalized profile ($L'_{\rm CO,a}/L'_{\rm CO,b} = 1$; equation 2), namely HerBS-69B, -120A, -120B, and -159B. Interestingly, these are found only in fields with multiple sources where the companion galaxy has a slightly different redshift. The large angular separation between the

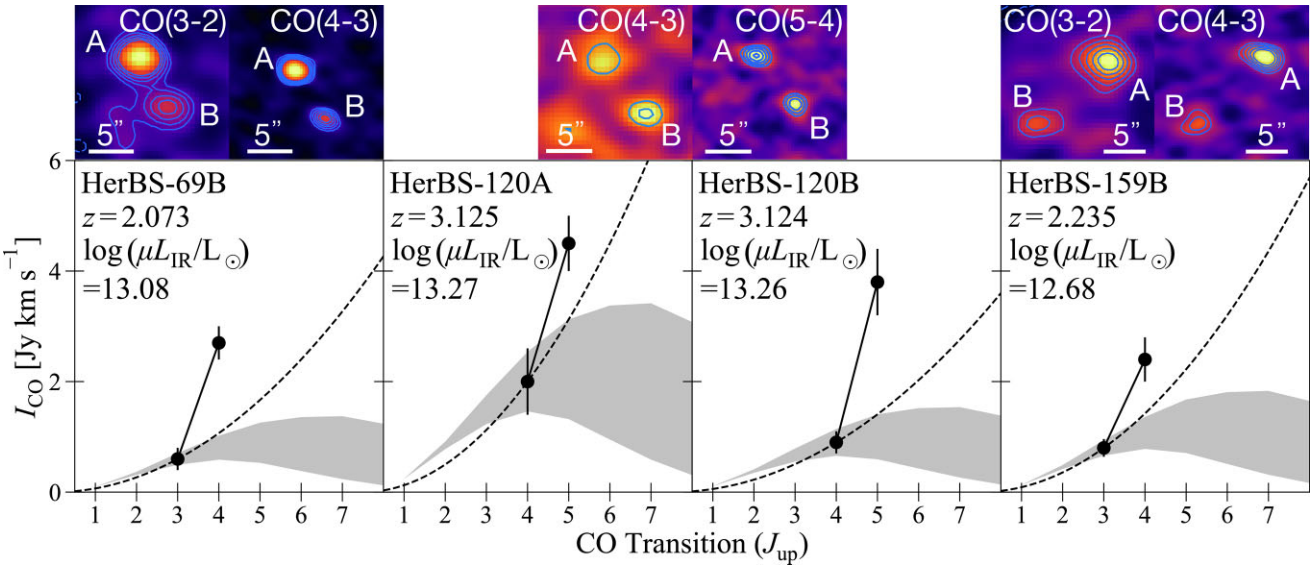

Figure 11. Four sources that have CO SLEDs in excess of a thermalized profile, where $L'_{\mathrm{CO,a}}/L'_{\mathrm{CO,b}} = 1$. All four have nearby sources at similar redshift. The *top panels* show the velocity-integrated fluxes of the spectral lines, with sources at more than 7 arcsec apart. The contours are drawn from 2σ for the left-hand panel and from 3σ for the right-hand panel. The white scale bar corresponds to 5 arcsec. The *bottom panels* show the CO SLEDs relative to the thermalized profile (*dashed black lines*) and the mean SLED with $\pm 1\sigma$ standard deviation from Harrington et al. (2021), similar to Fig. 1.

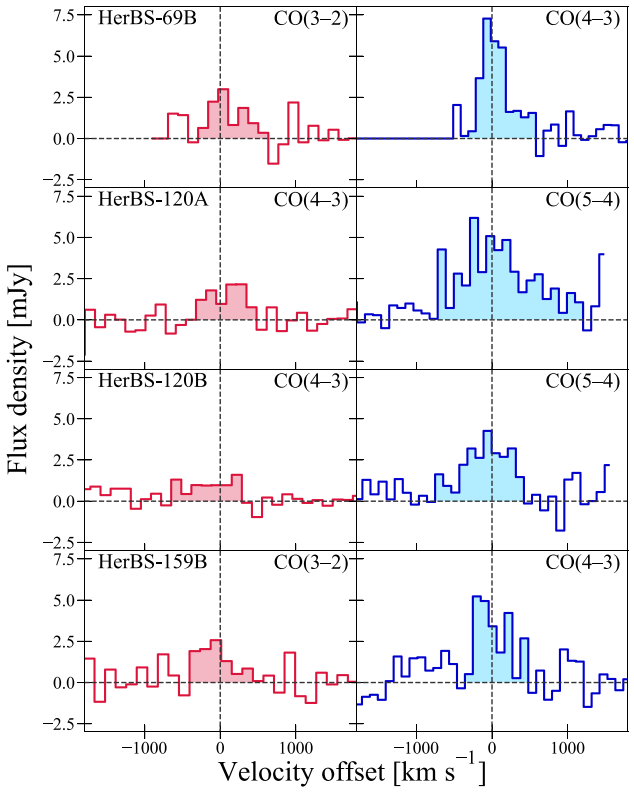

Figure 12. The spectra of four sources shown in Fig. 11. The *left-hand column* shows the lines in Band 3, and the *right-hand column* shows the lines in Band 4 for each source. *Colour filled regions* correspond to the velocity range where we make the velocity-integrated intensity maps. The horizontal axis shows the velocity offset from the systemic velocity ($V = 0$ km s^{-1}) obtained from the spectroscopic redshift. The spectral resolution is 0.05 GHz, which corresponds to ∼150 km s^{-1} for Band 3 and ∼100 km s^{-1} for Band 4.

components (7–10 arcsec) rules out galaxy–galaxy lensing, and the slightly different redshifts suggest they are not one source multiply imaged. In three out of four cases, they are the fainter component, i.e. B sources.[3] Fig. 11 shows the velocity-integrated CO intensity maps with contours (*top panels*) and individual SLEDs (*bottom panels*) of these four sources. The CO SLEDs are steeper than the thermalized SLED by about 1–2σ (and of course, they are above the mean SLED from Harrington et al. 2021). Fig. 12 shows the Bands 3 (*left-hand* column) and 4 (*right-hand* column) spectra of these four sources extracted with the same aperture size. Colour filled regions indicate the velocity range across which we make the velocity-integrated intensity maps (i.e. Fig. 11). The vertical dashed line of each panel corresponds to the systemic velocity obtained from the spectroscopic redshift. As expected, we find that the line fluxes in Band 3 are lower than those of Band 4.

5.1 Are we confident that these SLEDs are real?

We take several steps to ensure that the origins of these discrepant SLEDs are physical; we exclude statistical scatter in the ratios ($r_{a,b}$; equation 2), calibration issues, line-fitting issues, and issues associated with lensing.

Most of the galaxies in Urquhart et al. (2022) have 'normal' line ratios (see e.g. Fig. 3), while only six sources have values above unity, with two of these six sources consistent with a sub-thermal SLED. We measure the following luminosity ratios for these four sources: $r_{4,3} = 2.53 \pm 0.89$ for HerBS-69B; $r_{5,4} = 1.44 \pm 0.46$ for HerBS-120A; $r_{5,4} = 2.70 \pm 0.74$ for HerBS-120B; and $r_{4,3} = 1.69 \pm 0.44$ for HerBS-159B. As you can see, although these are consistent with thermalized profiles by 1–2.3σ, we note a fundamental limitation in assessing the super-thermalized line profiles using our data. We optimized the velocity-integrated fluxes of the lines to maximally

[3]For HerBS-69, the A source is 1.2 times brighter than the B source; for HerBS-120, the A source has a similar brightness as the B source; but for HerBS-159B, the A source is 3 times brighter than the B source.

include signal at a moderate cost in signal-to-noise ratio. This results in large intrinsic uncertainties in the luminosity ratios, since we are taking the ratio of two roughly 5σ luminosities. This limits the maximum significance in line ratios of around $3.5\sigma(\approx 5/\sqrt{2})$, as is seen in studies finding similar results (Riechers et al. 2006b, 2020; Weiß et al. 2007; Sharon et al. 2016). Moreover, we would rarely achieve a 3.5σ case, since we are identifying the super-thermalized cases by their line ratio being in excess of one (instead of zero). Although the luminosity ratios cannot exclude the explanation that these ratios are simple artefacts, the observed fluxes of the resolved lines (Fig. 12) show a more convincing case towards the veracity of the super-thermalized line profiles.

We estimate the potential for calibration issues by comparing the Bands 3 and 4 continuum emission from Bendo et al. (2023). The HerBS-120B source has 151 GHz to 101 GHz flux density ratio of 3.28. This is not extraordinary compared to other sources. For the other two fields (HerBS-69 and -159), we do not detect the Band 3 continuum; however, we confirm that the brighter sources in the same field, i.e. A sources have normal (sub-thermal) CO SLEDs. The photometric redshifts of the CUBS fields including ALMA Bands 3 and 4 agree with the spectroscopic solutions, and have similar uncertainties to other galaxies in the BEARS sample. The observational strategy in the BEARS programme images multiple galaxies using the same flux and phase calibrator, and here we note that HerBS-159 is observed in a different scheduling block than HerBS-120 and HerBS-69. The lack of any obvious calibration issues across the other sources in these scheduling blocks provides further confidence in the authenticity of these line ratios.

We also investigate potential issues with the line fitting. Based on Fig. 12, the CO emission lines are located at the band edge of our tunings for the HerBS-120 and HerBS-69 fields. We therefore investigate the off-source root mean square of the data cube as a function of frequency. We do not find any significant ($<$ 15per cent) variation in the noise at the position of the spectral lines. For HerBS-120A, the velocity width of both lines are different and thus we perhaps overestimate (underestimate) the line flux of Band 4 (Band 3).

We can also exclude differential magnification as an explanation, where the inhomogeneous magnification across the source causes flux ratios that are not representative of the entire source. The effects of differential magnification on CO SLEDs have been extensively simulated by Serjeant (2012). Flux from spatially concentrated regions can be located close to a caustics (i.e. high-magnification region), leading to higher magnifications than for the rest of the system. However, this boosting cannot explain why high-J CO transitions would appear to have super-thermal luminosities, because *all* transitions in the spatially concentrated region would be similarly boosted. Differential magnification of thermalized or sub-thermalized SLEDs only generates thermalized or sub-thermalized SLEDs. We provide a more thorough investigation why this is the case in Appendix E.

5.2 Physical interpretation

The conditions of the ISM affect the CO line ratios of galaxies. Higher- J CO lines trace denser gas components (with the CO line transitions having roughly $n_{\rm crit} \propto J^3$) and are often clumpy in nature, while the lower- J CO lines can extend throughout and even beyond individual galaxies (e.g. Cicone et al. 2021). Basic RADEX (van der Tak et al. 2007; Taniguchi 2020) models suggest that high hydrogen density ($> 10^4$ cm^{-3}) and high gas temperature ($T_{\rm kin} > 100$ K) can indeed reproduce such super-thermalized luminosity ratios until $\sim$1.7 between CO (4–3) and CO (3–2) as well as CO (5–4) and CO (4–3), which shows that there is no simple model reproducing the line luminosity ratio of $\gtrsim 2$. However, at least, these physical properties appear extreme when compared to previously observed gas conditions. Similar to differential lensing, a highly multiphased ISM cannot reproduce the observed ratios, as can be seen by evaluating the discussion in Appendix E with the magnification, μ, set to 1. To explain such extreme gas conditions we need strong heating sources, and thus we focus on dust-obscured active galactic nuclei (AGNs) or galaxy mergers.

Riechers et al. (2006b) presented similar super-thermalized luminosity ratios of CO (4–3) to CO (2–1) or CO (1–0) towards APM08279+5255, which is a lensed QSO at $z = 3.91$. Weiß et al. (2007) suggested that the luminosity ratio indicates moderate opacities of low-J CO transitions. Their large velocity gradient (LVG; Sobolev 1960) models also show that they can well explain that with $n_{\rm H} = 10^{4.2}$ cm^{-3} and $T_{\rm kin} = 220$ K, which is consistent with our RADEX model. Sharon et al. (2016) reported on observations of a total of 14 known lensed and unlensed sources using the *Karl G. Jansky* Very Large Array (VLA). They detected the CO (1–0) emission in 13 sources (down to low significance) and reported one non-detection. They found four candidates that show super-thermalized luminosity ratios between CO (3–2) and CO (1–0). Three of these are lensed AGN host galaxies, and the other is a lensed merging system. Sharon et al. (2016) noted large uncertainties in the luminosity ratios and provide several hypotheses to the high ratios: (i) the emission is optically thin; (ii) the CO (1–0) line is self-absorbed; and (iii) the source of optically thick emission has a temperature gradient. These hypotheses were also previously suggested by Bolatto et al. (2000, 2003), in addition to varying beam-filling factors across the different CO transitions, although filling factor effects would instead result in sub-thermalized CO line ratios. This latter point is not expected to be an issue with our current marginally resolved sources. Since our ratios do not include the CO (1–0) emission line, the second option is also not a likely solution, but the optical depth effects or thermal gradients can possibly explain our result. In the local Universe, Meijerink et al. (2013) suggested a potential explanation through shocks around the AGN for a local superthermalized candidate, NGC 6240. Here, we note that these previous works found discrepant luminosity ratios based on CO (1–0) – typically found to be more extended – so the reasons for the varying ratios might not be the same. Moreover, unlike other discrepant CO line ratio studies, we found these discrepant luminosity ratios using a single facility (ALMA), which makes the result less dependent on telescope-to-telescope variations.

AGN activity can heat gas and produce steep line intensity ratios out to (very) high CO line transitions (Riechers et al. 2006b; Weiß et al. 2007). An AGN with bolometric luminosity $> L_*$ would be vanishingly unlikely to be a companion galaxy based on the number densities in Shen et al. (2020) (1 arcmin area and $\delta z = 0.05$ spans 176 cMpc^3, compared to $\sim 10^{-5}$ cMpc^{-3} of $> L_*$ AGN) unless there is a causal factor in common with the DSFGs such as an environmental trigger or an interaction.

The super-thermalized ratios are observed solely for galaxies in systems of multiples. This could suggest that the presence of a nearby galaxy is important to produce the observed line ratios. Potentially, the interaction of merging galaxies could create the required high gas density and temperature conditions. The turbulent ISM resulting from galaxy mergers (or strong AGN winds) could affect the bulk gas (traced by the lower-J transitions) differently relative to the dense star-forming clumps (traced by the higher-J transitions). The larger line widths of the bulk gas would push down the optical depth for

a fixed column density, reducing the effective cross-section of the molecular gas clouds in the bulk gas and hence cause fainter emission from lower-*J* CO transitions. However, in our sample, the companion sources are at a projected distance of 50–80 kpc, which is large on the typical distance scales of merging systems (Narayanan et al. 2015).

5.3 BEARS: a unique parent sample?

Although we are unable to definitively exclude artefacts as the cause of these super-thermalized line profiles, we put these results into a larger cosmological perspective. These four sources are selected directly from the large, homogeneous sample from Urquhart et al. (2022), allowing us to infer the occurrence rate of DSFG properties. The typical lifetime of an DSFG (without excessive feeding; cf. Berta et al. 2021) is of the order of the depletion time, typically 200 Myr (e.g. Reuter et al. 2020 and this work). Our targets are four out of 46 galaxies with multiple CO lines from Urquhart et al. (2022) (i.e. 9 per cent), thus we can jointly constrain the time-scales and occurrence frequencies of these scenarios. For example, if AGNs are universal in DSFG environments, then the AGN lifetimes must be around 9 per cent of 200 Myr, while rarer companion AGNs must have longer lifetimes.

6 COMPOSITE SPECTRUM OF ALL BEARS SOURCES

The observations reported in Urquhart et al. (2022) directly detected CO (2–1) to CO (7–6) lines, as well as the two transitions of [C I] emission and the H_2O (2_{11}–2_{02}) water line. In this section, we aim to statistically detect more emission lines by stacking the spectrum for each galaxy in their rest frames. This is similar to work on the SPT galaxies (e.g. Spilker et al. 2014; Reuter et al. 2020, 2022), as well as for *Herschel* (Fudamoto et al. 2017), LABOCA (Birkin et al. 2021), and SCUBA-2 (Chen et al. 2022) selected sources. In this section, we aim to provide the archetypal spectrum of a hypothetical galaxy at a redshift of 2.5 with an observed infrared luminosity of 3×10^{13} $L_\odot$.

6.1 Method

We now re-extract the spectral data from the individual data cubes of the sources using an automated script. This evenly extracts the spectroscopic information for fair comparison of the bulk behaviour of all galaxies, although it prioritizes signal-to-noise over including all possible signal. Using the central positions of the continuum peak positions reported in Bendo et al. (2023), we extract the emission with a variable aperture between 1 and 3 times the radius of the beam to find the optimal balance between high signal-to-noise and full line extraction.

Fig. 13 shows the effective flux and signal-to-noise of the CO (2–1) to CO (7–6), [C I] ($^3P_1$–$^3P_0$), [C I] ($^3P_2$–$^3P_1$), and H_2O lines in an effort to find the optimum extraction area for the automated pipeline. The lines are evaluated within a 600 km s^{-1} bin; a bin width that was similarly chosen to include most of the signal while also achieving a high signal-to-noise ratio (see Section 6.2). We find the best extraction aperture to lie at twice the radius of the beam. With only marginal losses in signal-to-noise ratio ($\approx 13\pm 5$ per cent), the majority of the flux is extracted across all the lines ($\approx 92\pm 6$ per cent). Beyond this size, there appears a sharp down-turn in signal-to-noise ratio complicating the goal of the composite spectrum – to reveal faint line emission. We correct the stacked spectrum by boosting the flux by 8 per cent (=1/0.92), and accounting for 6 per cent extra noise in the extracted values, added in quadrature.

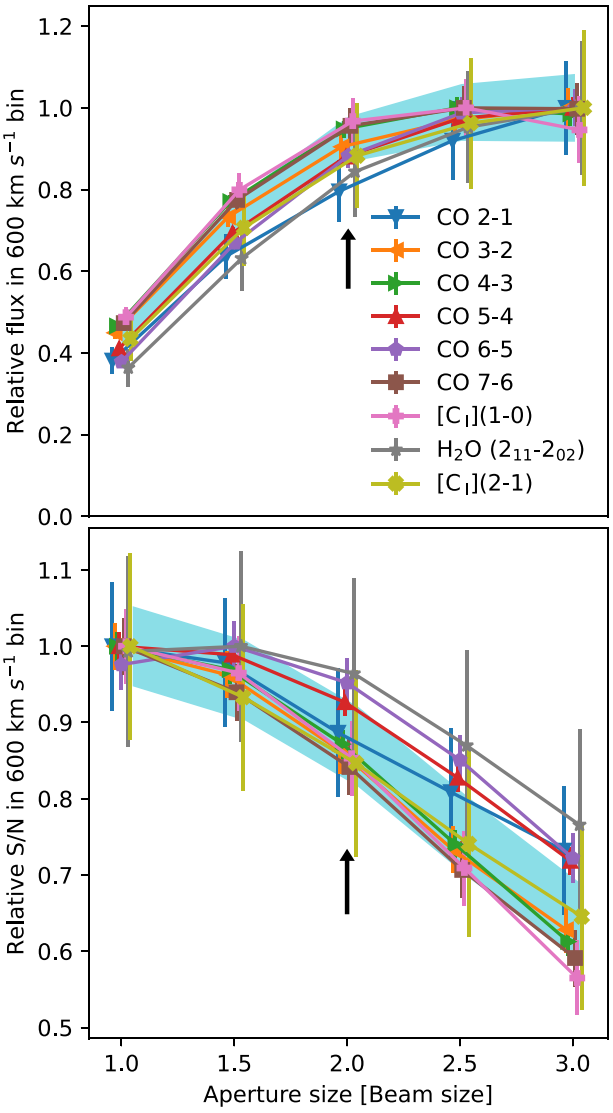

Figure 13. Spectral line fluxes (*top*) and SNRs (*bottom*) measured within 600 km s^{-1} bins versus the aperture size (in FWHM) plotted for multiple spectral lines. The *points* indicate individual spectral lines, and the *background fill* indicates the averaged relative flux (*top*) and SNR (*bottom*). We choose the extraction sizes of our apertures carefully, by balancing between a large enough aperture to include all the flux, while not degrading our signal-to-noise excessively. Hence, we decide to use an aperture with twice the radius as the beam (*arrow*). At this frequency, we are able to extract 92 ± 6 per cent of the flux density at a cost of 13 ± 5 per cent additional noise.

We subtract the continuum emission directly from the spectra assuming a power-law dust continuum emission ($S_\nu = A_i \nu^{(2+\beta)}$), with $\beta_{\rm dust} = 2$. We separately fit the spectra from Bands 3 and 4, while masking out the data within 1500 km s^{-1} around the CO, [C I], and H_2O lines. We compare to the 151 GHz continuum fluxes from Bendo et al. (2023), and we find a general agreement to their fluxes. On average, our flux estimates agree with the 151 GHz continuum fluxes, and we find a point-to-point standard deviation of 11 per cent, although the scatter decreases for the brightest sources (to around 5 per cent).

We decide to stack the spectrum of each galaxy with the goal of representing a single archetypal galaxy at $z = 2.5$ (approximately the mean of this sample; Urquhart et al. 2022) with an infrared luminosity of 3×10^{13} $L_\odot$. This involves normalizing all spectra to the same luminosity and to a common redshift. We use the same scaling factor as Spilker et al. (2014), which is derived from requiring a constant L' across all redshifts in equation (1):

$$S_{\nu,\mathrm{common}} = S_\nu \left(\frac{D_\mathrm{L}(z_\mathrm{source})}{D_\mathrm{L}(z_\mathrm{common})} \right)^2 \frac{1+z_\mathrm{common}}{1+z_\mathrm{source}}, \quad (11)$$

where D_L refers to the luminosity distance at redshift z, and z_common is set to 2.5. This factor accounts for the cosmological dimming for each spectral line, as well as for the redshift dependence of the flux density unit.

We then normalize the luminosity of each galaxy to 3×10^{13} $L_\odot$, based on the luminosities calculated in Section 4.2. Since source confusion could affect the *Herschel* photometry, we take the 151-GHz flux density that is detected for all sources, and assume a dust temperature T_d of 35 K.[4] Here, we note several important caveats when creating a combined spectrum from sources across different frequencies, luminosities, and redshifts. Unlike previous methods, we provide a stacked spectrum normalized against the intrinsic properties of the observed galaxies. Previous methods provide their composite spectrum based on observed properties (e.g. Spilker et al. 2014 aim to provide the properties of a $z = 3$ SPT galaxy with $S_{1.4\mathrm{mm}} = 15$ mJy). This is an important point since even at 1.4 mm, a source with constant flux-density undergoes a roughly 40 per cent luminosity difference between $z = 1$ and $z = 5$, despite the near-flat K-correction with redshift at 1.4 mm (and in our case 2 mm). This results in a noticeable effect on a composite spectrum because each part of the rest-frame spectrum is sensitive to sources from different redshift regions. The luminosity variations with redshift cause an underestimate of the flux at higher redshifts compared to lower redshifts and produces an artificial SLED with a downward slope towards higher-J, estimated in Spilker et al. (2014) to be $\simeq$ 15 per cent. These choices make their stacked spectrum a representation of the average observed behaviour of an SPT galaxy. However, their line luminosities do not represent a single (hypothetical) galaxy across all frequencies and the CO line fluxes thus do not represent a typical CO SLED (Reuter et al. 2022). We note that Birkin et al. (2021) and Chen et al. (2022) use a median or averaged spectrum based solely on the highest signal-to-noise emission. This provides an accurate picture of the average observational result for a galaxy in the sample, but does not reflect the average properties of any single existing or archetypal galaxy.

The stacked spectrum is created at several velocity resolutions by adding the rest-frequency spectra of each source, corrected for luminosity and redshift. Each spectrum is additionally weighted by the inverse variance in each channel. This final weighting step ensures a high signal-to-noise in the stacked spectrum, and removes much of the weighting by luminosity (3×10^{13} $L_\odot$) and redshift ($z_\mathrm{common} = 2.5$) per each line (or any other weighting based on the properties of a galaxy, i.e. observed flux density or dust mass). In other words, the galaxy-based weighting step affects the ratios between lines, while the noise-based weighting ensures a high signal-to-noise across the spectrum.

We estimate the noise properties of our stacked spectrum using the following procedure. We extract the signal-to-noise ratio in 5000 bins of 600 km s^{-1} width at random off-line frequencies. Fig. 14 shows this signal-to-noise distribution, where the frequencies of the bins are chosen to not overlap with any known lines (see Appendix Table F1). The *dashed black and white line* reflects a unit-width Gaussian profile, and accurately describes the histogram. The off-line stacked spectrum is thus well described by a white noise spectrum, and importantly confirms there are no issues with coherent processes with our spectrum, such as imperfect continuum subtraction.

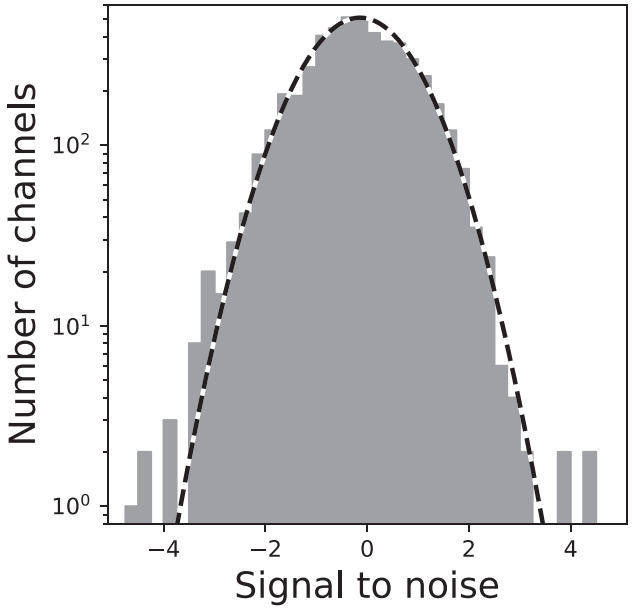

Figure 14. Histogram of 5000 signal-to-noise measurements in off-line 600 km s^{-1} bins of the stacked spectrum. The *dashed black-and-white line* indicates the unit-width Gaussian profile, which matches the bulk of the signal-to-noise distribution well. There exist some excess bins at both low and high signal-to-noise ratio, although there are very few of these.

6.2 Results

We show the composite spectrum in Fig. 15. The top panel shows the spectrum in bins of 300 km s^{-1} from 220 to 890 GHz. The middle panel shows the signal-to-noise ratio of the stacked spectrum with the same binning. The bottom panel shows the number of sources contributing to the stacked spectrum as a function of frequency. Fig. 16 shows the zoomed-in spectra of the detected lines. The Gaussian fit parameters are shown in Table 1.

Similar to the work of Spilker et al. (2014), we use per-line bins to extract any potential line emission that is missed by the stacked spectrum. The composite spectrum could miss any emission by *smearing* flux across more than one spectral bin, especially since the bins are not necessarily centred on the positions of the line emission. Instead, we explore the optimum emission line by comparing the SNR of the highest-SNR line, CO (5–4), across every velocity spacing between 200 and 1000 km s^{-1} at 50 km s^{-1} increments. The highest SNR of the velocity-integrated flux is found at a bin size of 600 km s^{-1}. In a final attempt to optimally extract spectral lines, we stack all covered transitions of each line. We stack in L' to correctly preserve the luminosity comparison of the ratios in L' units (see equation 11). The result is shown in Table 2, and zoom-ins on individual lines are shown in Fig. 16.

Table F1 shows the resulting L' estimates for 117 spectral lines within the 220–890 GHz composite spectrum. In order to optimally

[4]For a comparison to the line luminosities in Spilker et al. (2014), one can multiply our L' values by 1.67 to compare our line luminosities to theirs.

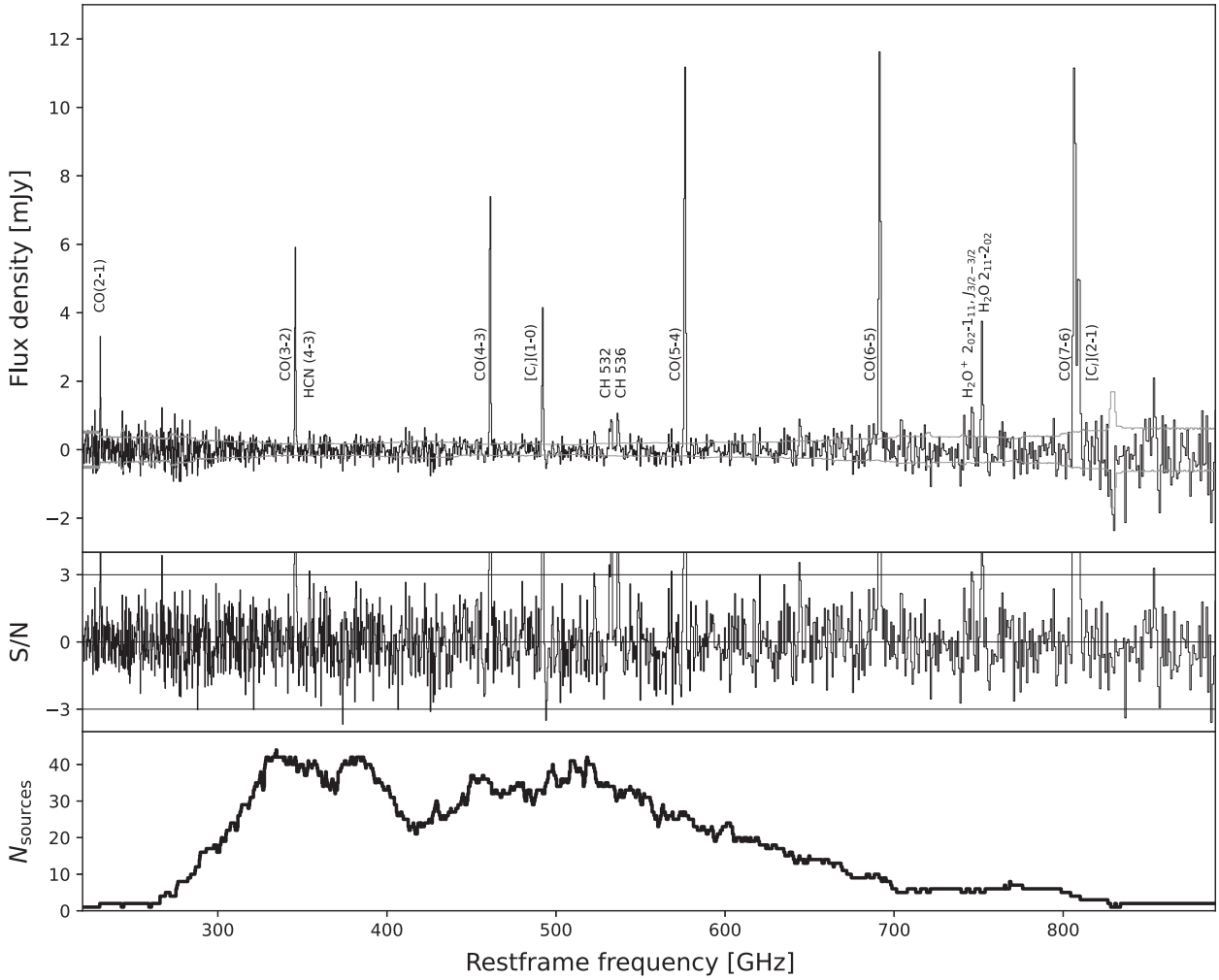

Figure 15. *Top panel:* Rest-frame composite spectrum between 220 and 890 GHz in 300 km s^{-1} bins, combining the data of the 71 galaxies in our sample. This spectrum is scaled such that it is representative of a *typical* 3×10^{13} L$_\odot$ BEARS galaxy at $z = 2.5$. We show the $\pm 1\sigma$ standard deviation with a *thin grey* line. In addition to the CO, [C I] and water lines, we find indications for CH emission in both the 532 and 536 transition, as well as H_2O^+ emission. Zoom-ins on these lines are shown in Fig. 16. *Middle panel:* Signal-to-noise ratios for lines across the entire composite spectrum. The *horizontal lines* show the plus and minus 3σ confidence ranges. *Bottom panel:* Number of sources that contribute to the composite spectrum, as a function of rest-frame frequency. The low- and high-frequency tails of the spectrum rely on single-digit numbers of sources, with the central 300–700 GHz region combining between 10 and 45 galaxies in each 300 km s^{-1} bin.

detect single species, we combine the bins of all transitions in ^{13}CO, C^{18}O, HCN, HNC, HCO$^+$, and CH. The emission of several lines is potentially overlapping, particularly affecting the observed emission at the frequencies of CH 532 and HCN (6–5), as well as CH 536 and HOC$^+$ (6–5). In this case, we follow the results from local ULIRGs by Rangwala et al. (2014), and attribute the majority of the signal to the CH lines. All lines reported in the stacked spectrum, shown in Fig. 15, are also seen in the bin-optimized extraction.

The CO line ratios from the composite spectrum agree with the other CO SLEDs (e.g. Harrington et al. 2021) and the individual galaxies, as seen in Figs 2 and 4. The combined line emission of all CO lines adds to over 100σ. This allows us to look for large velocity tails in the emission of the spectral lines. Feeding and feedback are important components to the evolutionary track of high-redshift galaxies (Péroux & Howk 2020; Berta et al. 2021), and are sometimes revealed through wide velocity line profiles (Ginolfi et al. 2020). At high redshift, outflow signatures are typically seen in [C II] (Fujimoto et al. 2019, 2020; Ginolfi et al. 2020; Herrera-Camus et al. 2021; Izumi et al. 2021) and might not be visible in (higher-J transitions of) CO lines, although Cicone et al. (2021) found an extended CO halo at $z \sim 2$ at velocities beyond 1000 km s^{-1}. However, for our sample, both single-Gaussian fitting (Table 1) and visual inspection of the stacked lines (Fig. 16) do not show any large velocity components above 3σ. Our findings are in line with the recent stacking work by Birkin et al. (2021), which also fails to reveal any high-velocity tails, as well as in Meyer et al. (2022) who emphasize the need for accurate continuum subtraction when comparing high-velocity tails.

^{12}CO lines can reach optically thick column densities, but the isotopologues of CO often stay optically thin. As such, the line ratios can be a useful probe of the optical depth. No individual CO isotopologues have been detected. Similarly, the combined stack of both ^{13}CO and C^{18}O shows no significant emission. The resulting line ratio lower limits for $L'_{^{12}\mathrm{CO}}/L'_{^{13}\mathrm{CO}}$ and $L'_{^{12}\mathrm{CO}}/L'_{\mathrm{C}^{18}\mathrm{O}}$ are > 35. The $L'_{^{12}\mathrm{CO}}/L'_{^{13}\mathrm{CO}}$ line ratio lower limit is around 2 times higher than observed for the SPT galaxies (Spilker et al. 2014), although the relative errors are substantial. The $L'_{^{12}\mathrm{CO}}/L'_{\mathrm{C}^{18}\mathrm{O}}$ line ratio also remains undetected in the SPT survey, in line with our results. The

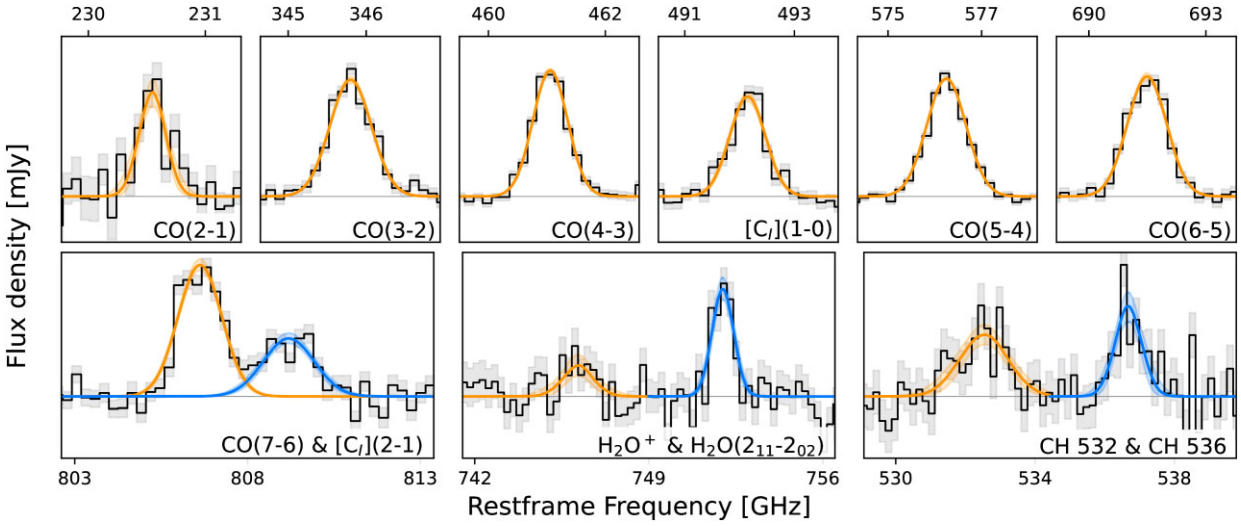

Figure 16. Stacking results for individual lines at the 70 km s^{-1} resolution. We fit the line profiles of each line with a Gaussian, and provide the fitted line properties in Table 1. No obvious extended emission is seen in the combined profiles, similar to previous works that focused on stacking of DSFGs (e.g. Birkin et al. 2021).

Table 1. Line properties fitted to the 70 km s^{-1} stacked spectrum.

Line	$S\delta V$ (Jy km s^{-1})	δV (km s^{-1})	Luminosity (10^7 L$_\odot$)
CO ($J = 2$–1)	$1.71^{+0.22}_{-0.22}$	353^{+73}_{-63}	$5.12^{+0.66}_{-0.66}$
CO ($J = 3$–2)	$3.71^{+0.11}_{-0.11}$	542^{+19}_{-18}	$16.65^{+0.49}_{-0.49}$
CO ($J = 4$–3)	$4.52^{+0.09}_{-0.09}$	453^{+10}_{-10}	$27.05^{+0.54}_{-0.54}$
CO ($J = 5$–4)	$7.07^{+0.11}_{-0.10}$	517^{+9}_{-9}	$52.89^{+0.82}_{-0.75}$
CO ($J = 6$–5)	$7.15^{+0.18}_{-0.18}$	511^{+16}_{-15}	$64.18^{+1.62}_{-1.62}$
CO ($J = 7$–6)	$7.59^{+0.31}_{-0.31}$	558^{+28}_{-26}	$79.5^{+3.25}_{-3.25}$
[C I] ($^3P_1$–$^3P_0$)	$2.17^{+0.10}_{-0.09}$	469^{+26}_{-25}	$13.86^{+0.64}_{-0.57}$
[C I] ($^3P_2$–$^3P_1$)	$3.90^{+0.32}_{-0.34}$	645^{+67}_{-60}	$40.97^{+3.36}_{-3.57}$
CH 532	$0.91^{+0.14}_{-0.14}$	928^{+209}_{-171}	$6.29^{+0.97}_{-0.97}$
CH 536	$0.72^{+0.13}_{-0.12}$	522^{+147}_{-119}	$5.02^{+0.91}_{-0.84}$
H_2O^+ 746	$0.81^{+0.51}_{-0.30}$	582^{+2764}_{-256}	$7.85^{+4.94}_{-2.91}$
H_2O (2_{11}–2_{02})	$1.83^{+0.21}_{-0.21}$	408^{+54}_{-48}	$17.86^{+2.05}_{-2.05}$

Table 2. Stacks of line types.

Line	$N_{\rm observations}$	Line luminosity (10^9 K km s^{-1} pc^2)	SNR
CO	120	$\mathbf{62.5 \pm 3.6}$	(103.1σ)
^{13}CO	122	0.5 ± 0.6	(0.9σ)
C^{18}O	126	0.9 ± 0.6	(1.5σ)
[C I]	36	$\mathbf{24.8 \pm 1.7}$	(25.6σ)
HCN	140	1.4 ± 0.5	(2.7σ)
HNC	135	0.9 ± 0.6	(1.6σ)
HCO$^+$	137	0.7 ± 0.5	(1.3σ)
HOC$^+$	132	1.5 ± 0.6	(2.6σ)
CH	65	$\mathbf{7.3 \pm 0.9}$	(8.7σ)
H_2O^+	98	0.3 ± 0.4	(0.7σ)
SiO	273	-0.1 ± 0.4	(-0.2σ)
CS	218	0.5 ± 0.5	(1.0σ)
NH_3	152	-0.0 ± 0.5	(-0.1σ)
CCH	133	-0.5 ± 0.6	(-0.8σ)
H21–28α	220	0.1 ± 0.5	(0.3σ)

transitions of the CO isotopologues are often observed together with the detected ^{12}C^{16}O line transitions, which increases the robustness of our upper limits, because we are comparing like-for-like transitions for each galaxy in our isotopologue ratio estimates.

Our isotopologue results are within the typical range of other galaxies, although local molecular clouds typically have lower ratios. The Milky Way's molecular clouds have $L'_{^{12}\rm CO}/L'_{^{13}\rm CO}$ ratios between 5 and 10 (Buckle et al. 2010, 2012), although the chemical abundances of the carbon element (^{12}C to ^{13}C) evolves from 25 near the Galactic Centre up to 100 in the solar vicinity (Wilson & Rood 1994; Wang et al. 2009). Cao et al. (2017) and Cormier et al. (2018) report on spiral galaxies, with average ratios between 8 and 20. The local ULIRG Arp 220 has different isotopologue line ratios depending on the transition, ranging from 40 down to 8 (Greve et al. 2009) for ^{13}CO (1–0) to (3–2), and a $L'_{^{12}\rm CO}/L'_{\rm C^{18}O}$ ratio of 40 for C^{18}O (1–0). Similarly, Sliwa et al. (2017) find 60 to 200 for the $L'_{^{12}\rm CO}/L'_{^{13}\rm CO}$ and $L'_{^{12}\rm CO}/L'_{\rm C^{18}O}$ ratios for the nearby ULIRG IRAS 13120−5453.

Higher-redshift galaxies also show relatively diverse isotopologue line ratios, with Méndez-Hernández et al. (2020) finding 16 and 40 for $L'_{^{12}\rm CO}/L'_{^{13}\rm CO}$ and $L'_{^{12}\rm CO}/L'_{\rm C^{18}O}$, respectively, for a sample of star-forming galaxies at $z \approx 0.02$–0.2. The DSFG Cosmic Eyelash (SMM J2135 − 0102) has an $L'_{^{12}\rm CO}/L'_{^{13}\rm CO}$ ratio in excess of 60, with similarly luminous $L'_{\rm C^{18}O}$. The Cloverleaf quasar (Henkel et al. 2010) shows a high ^{13}CO flux, with an associated ratio of 40. Individual observations of two SPT sources (Béthermin et al. 2018) find a line ratio of around 26 for $L'_{^{12}\rm CO}/L'_{^{13}\rm CO}$, and Zhang et al. (2018) report $L'_{^{12}\rm CO}/L'_{^{13}\rm CO}$ ratios of 19–23 and $L'_{^{12}\rm CO}/L'_{\rm C^{18}O}$ ratios between 25 and 33. Our BEARS targets appear to agree with the more actively star-forming or AGN-dominated systems in the local and high-redshift Universe, which are suggestive of optically thick emission, although the spatial variation of the isotopologue emission can cause filling factor effects (e.g. Aalto et al. 1995).

The relative ratios of the isotopologues to one another can further reveal the star-forming conditions of the system (Davis 2014; Jiménez-Donaire et al. 2017). The nucleosynthesis of the carbon and oxygen isotopes are both produced in the CNO cycle (Maiolino & Mannucci 2019). The carbon isotope is formed through intermediate

stars, on typical time-scales of > 1Gyr, while the oxygen isotope is produced through more massive stars (Henkel & Mauersberger 1993; Wilson & Rood 1994). Both at low and high redshift, low ratios of $L'_{^{13}CO}/L'_{C^{18}O}$ can be interpreted as an effect of a variable IMF. For example, Sliwa et al. (2017) report ratios below 1 for $L'_{^{13}CO}/L'_{C^{18}O}$ for the local ULIRG IRAS 13120−5453, and Zhang et al. (2018) find that only a top-heavy IMF can produce the observed low ratios of $L'_{^{13}CO}/L'_{C^{18}O}$. Our stacked observations are unable to detect this line ratio, although we are likely close to the detection limit of (one of the two) isotopologues given the existing detections in similar sources. These stacking observations argue towards the need for detailed and individual studies of isotopologues at high redshift, particularly of the brightest sources, instead of stacking studies across multiple sources.

The observed [C I] ($^3P_1$–$^3P_0$) and [C I] ($^3P_2$–$^3P_1$) line luminosities correlate with infrared luminosities for our sources, as well as local and other high-redshift galaxies over five orders of magnitude (Fig. 4). The detection of neutral carbon and CO lines furthermore enables a comparison to PDR models and the line ratios of our stacked spectrum provide similar FUV radiation field and gas density values as the average sample, as seen in Fig. 9.

These stacking attempts reveal HCN (4–3), and tentatively show a small feature near the CH 532 associated with HCN (6–5) in Fig. 16, also noticeable in the larger velocity width of the CH 532 in Table 1 ($\delta V \approx 928$ km s^{-1}). These transitions suggest the presence of dense gas, since their critical density is about 100–1000 larger than those of CO lines (10^{9-10} cm^{-3}; Jiménez-Donaire et al. 2019; Lizée et al. 2022), and thus could be associated with dense star-forming regions (Goldsmith & Kauffmann 2017) or with AGNs (Aalto et al. 2012; Lindberg et al. 2016; Cicone et al. 2020; Falstad et al. 2021). HCN is incidentally detected in the brightest high-redshift galaxies (Riechers et al. 2006a, 2010; Oteo et al. 2017; Cañameras et al. 2021). In contrast, Rybak et al. (2022) reported one detection of HCN (1–0) emission line as a result of a deep survey with VLA towards six strongly lensed DSFGs. They suggest that in fact most DSFGs have low-dense gas fraction. When stacking all the HCN lines across the entire sample, 140 line transitions are stacked, resulting in a 2.7σ tentative feature of 1.4×10^9 K km s^{-1} pc^2. We obtain the HCN/CO line luminosity ratio of $L'_{HCN}/L'_{CO} = 0.022 \pm 0.008$ and an upper limit on the HCO$^+$/CO line luminosity ratio of $L'_{HCO^+}/L'_{CO} < 0.024$ based on our stacked spectrum. The deep VLA survey from Rybak et al. (2022) reports an upper limit in line luminosity ratio of $L'_{HCN}/L'_{CO} < 0.045$ and $L'_{HCO^+}/L'_{CO} < 0.043$, using solely the ground transitions. Since our results use a stack across multiple higher order transitions, a direct comparison between these results is more difficult, however, our results also suggest a dearth of dense gas in the BEARS sample. No other cyanide molecules nor the radical are detected. The individual and stacked lines agree with the observed line luminosities from Spilker et al. (2014), and suggest that dense star-forming regions are present across most DSFGs.

Five sources are observed at the rest-frame frequency of the H_2O (2_{11}–2_{02}) line. The average line-to-total-infrared luminosity ratio is in line with the scaling relations of Jarugula et al. (2021) and Yang et al. (2016), as well as the one fitted to our data. The scaling relation found in Section 4.8 is instead due to the lower water line luminosity seen in infrared-fainter galaxies. The detection of H_2O^+ 746 allows us to make a rough estimation of the cosmic ray ionization rate. We find a luminosity ratio of $H_2O^+/H_2O \approx 0.4 \pm 0.2$, which is in agreement with Yang et al. (2016) ($H_2O^+/H_2O \approx 0.3 \pm 0.1$). The predicted ionization rate (Meijerink et al. 2011) is around 10^{-14} to 10^{-13} s^{-1}.

The bright emission from the CH doublet at 532 and 536 GHz indicates the existence of high-density gas in X-ray-dominated regions (XDRs) associated with bright stars or AGNs (Meijerink, Spaans & Israel 2007; Rangwala et al. 2014) or strong irradiation through cosmic rays (Benz et al. 2016). Currently, the two scenarios are not easily distinguished (Wolfire, Vallini & Chevance 2022), although enhanced excitation of high-J CO lines through (resolved) observations could favour an XDR origin (Vallini et al. 2019), taking into account the effect of mechanical shock excitation of the high-J CO components (Meijerink et al. 2013; Falgarone et al. 2017). Regardless of the origin of the CH 532 and 536 line emission, strong radiation sources and/or cosmic rays are necessary to explain the nature of these distant DSFGs.

7 CONCLUSIONS

We have investigated the physical properties of the BEARS sample, which consists of 71 line-detected galaxies, based on 156 spectral line flux estimates including upper limits (the detections of 117 CO, 27 [C I], and two H_2O lines, and the upper limits of a single CO, six [C I], and three H_2O lines). We report the following conclusions:

(i) The average gas properties of our sample are similar to other DSFG samples. Especially, the CO SLEDs of most sources as well as the stacked CO SLED follows the mean CO SLED for *Planck*-selected lensed DSFGs from Harrington et al. (2021).

(ii) Our galaxies follow the relation between line luminosity and infrared luminosity over five orders of magnitude when compared to reference samples at low and high redshift. The SK relation, however, shows that our sources and other DSFGs are not located in same star formation phase as local and low-redshift gas-rich, normal star-forming systems. In addition, our sources seem to have slightly longer depletion times than other DSFGs from Chen et al. (2017), although this effect could be explained by a difference in the size estimation of the star-forming regions.

(iii) Most of our samples have dynamical masses between 10^{11} and 10^{12} M$_\odot$ and are found to be lower than molecular gas mass estimates. This means that we likely underestimate the dynamical mass within the BEARS systems. This could be caused by differential lensing or because these systems are dynamically complex.

(iv) The dust-to-gas ratios of our sources do not vary with redshift, and the ratios are similar to that of the Milky Way. The low scatter and lack of trend with redshift suggest we are witnessing a single star-forming phase, and the high dust-to-gas ratio suggests that this phase occurred relatively recently.

(v) The PDR conditions of the BEARS sources are similar to those of DSFGs and local U/LIRGs, with denser and more intense radiation environments than low-z MS galaxies in line with previous studies (e.g. Valentino et al. 2020b). We investigate these PDR conditions with `PDRT` and find that most of our galaxies are located within $10^4 \leq n_H \leq 10^5$ [cm^{-3}] and $10^3 \leq G_0 \leq 10^4$ [Habing].

(vi) Our linear regression fitting of the H_2O (2_{11}–2_{02}) to infrared luminosity relation for low- and high-redshift samples favours a super-linear relation with 3σ significance, consistent with previous observations from Yang et al. (2016).

(vii) We find four candidates (HerBS-69B, -120A, -120B, and -159B) that show 'super-thermalized' CO line ratios. Although their ratios are consistent with thermalized one at 1–2.3σ due to the large uncertainty inherent in luminosity ratio estimates, especially, HerBS-69B and -120B stand out from the other 44 galaxies, suggesting a rare phase in the evolution of DSFGs. We note that we require follow-up observations to confirm their super-thermalized nature.

(viii) The deep stacked spectrum (220–890 GHz) reveals an additional H_2O^+ line, as well as the dense gas tracer HCN (4–3), and two tracers of XDR and/or cosmic-ray-dominated environments through CH 532 and 536. The total stack provides deep upper limits on the ^{13}CO and $C^{18}O$ isotopologues, in line with previous observations and line stacking experiments.

In the near future, we aim to expand upon the current studies with high-resolution imaging to reveal the morphological and kinematic properties of these galaxies. We place a particularly focus on the CUBS targets to confirm their super-thermalized line profiles, using tracers that reveal merging or AGN activity, as well as the highest-resolution imaging possible using the near-infrared *JWST*. Further continuation of the study of the ISM of these galaxies is also necessary, notably towards water and carbon emission lines. Finally, an important goal is the redshift completion of the sample targeted in Urquhart et al. (2022).

ACKNOWLEDGEMENTS

We would like to thank the anonymous referee for their insightful comments and suggested additions. This work was supported by the National Astronomical Observatory of Japan (NAOJ) ALMA Scientific Research Grant nos. 2018–09B and Japan Society for the Promotion of Science (JSPS) KAKENHI nos. 17H06130, 22H04939, and 22J21948. SS was partly supported by the ESCAPE project; ESCAPE—The European Science Cluster of Astronomy and Particle Physics ESFRI Research Infrastructures has received funding from the European Union's Horizon 2020 research and innovation programme under grant agreement no. 824064. SS also thanks the Science and Technology Facilities Council for financial support under grant ST/P000584/1. SU would like to thank the Open University School of Physical Sciences for supporting this work. HU acknowledges support from JSPS KAKENHI Grant Number 20H01953. CY acknowledges support from European Research Council (ERC) Advanced Grant 789410. HD acknowledges financial support from the Agencia Estatal de Investigación del Ministerio de Ciencia e Innovación (AEI-MCINN) under grant (La evolución de los cíumulos de galaxias desde el amanecer hasta el mediodía cósmico) with reference (PID2019-105776GB-I00/DOI:10.13039/501100011033) and acknowledge support from the Agencia Canaria de Investigación, Innovación y Sociedad de la Información (ACIISI), Consejería de Economía, Conocimiento y Empleo del Gobierno de Canarias, and the European Regional Development Fund (ERDF) under grant with reference PROID2020010107.

DATA AVAILABILITY

The *Herschel* SPIRE data can be downloaded from https://www.h-atlas.org, while the reduced, calibrated and science-ready ALMA data are available from the ALMA Science Archive at https://almascience.eso.org/asax/.

REFERENCES

Aalto S., Booth R. S., Black J. H., Johansson L. E. B., 1995, A&A, 300, 369
Aalto S., Garcia-Burillo S., Muller S., Winters J. M., van der Werf P., Henkel C., Costagliola F., Neri R., 2012, A&A, 537, A44
Alaghband-Zadeh S. et al., 2013, MNRAS, 435, 1493
Apostolovski Y. et al., 2019, A&A, 628, A23
Aravena M. et al., 2016, MNRAS, 457, 4406
Bakx T. J. L. C., Dannerbauer H., 2022, MNRAS, 515, 678
Bakx T. J. L. C. et al., 2018, MNRAS, 473, 1751
Bakx T. J. L. C., Eales S., Amvrosiadis A., 2020a, MNRAS, 493, 4276
Bakx T. J. L. C. et al., 2020b, MNRAS, 494, 10
Bakx T. J. L. C. et al., 2020c, MNRAS, 496, 2372
Barnes J. E., Hernquist L. E., 1991, ApJ, 370, L65
Barro G. et al., 2016, ApJ, 827, L32
Bendo G. J. et al., 2023, preprint (arXiv:2301.02584)
Benz A. O. et al., 2016, A&A, 590, A105
Berta S. et al., 2021, A&A, 646, A122
Béthermin M. et al., 2018, A&A, 620, A115
Birkin J. E. et al., 2021, MNRAS, 501, 3926
Bisbas T. G., Bell T. A., Viti S., Yates J., Barlow M. J., 2012, MNRAS, 427, 2100
Bisbas T. G., van Dishoeck E. F., Papadopoulos P. P., Szűcs L., Bialy S., Zhang Z.-Y., 2017, ApJ, 839, 90
Blain A. W., Smail I., Ivison R. J., Kneib J.-P., Frayer D. T., 2002, Phys. Rep., 369, 111
Blain A. W., Chapman S. C., Smail I., Ivison R., 2004, ApJ, 611, 725
Boggs P. T., Byrd R. H., Rogers J. E., Schnabel R., 1992, User's reference guide for ODRPACK version 2.01:: software for weighted orthogonal distance regression, https://doi.org/10.6028/NIST.IR.4834
Bolatto A. D., Jackson J. M., Israel F. P., Zhang X., Kim S., 2000, ApJ, 545, 234
Bolatto A. D., Leroy A., Israel F. P., Jackson J. M., 2003, ApJ, 595, 167
Bolatto A. D., Wolfire M., Leroy A. K., 2013, ARA&A, 51, 207
Boogaard L. A. et al., 2020, ApJ, 902, 109
Bothwell M. S. et al., 2013, MNRAS, 429, 3047
Bothwell M. S. et al., 2017, MNRAS, 466, 2825
Bouché N. et al., 2007, ApJ, 671, 303
Buckle J. V. et al., 2010, MNRAS, 401, 204
Buckle J. V. et al., 2012, MNRAS, 422, 521
Bussmann R. S. et al., 2013, ApJ, 779, 25
Bussmann R. S. et al., 2015, ApJ, 812, 43
Butler K. M. et al., 2021, ApJ, 919, 5
Cai Z.-Y. et al., 2013, ApJ, 768, 21
Cañameras R. et al., 2018, A&A, 620, A61
Cañameras R. et al., 2021, A&A, 645, A45
Cao Y., Wong T., Xue R., Bolatto A. D., Blitz L., Vogel S. N., Leroy A. K., Rosolowsky E., 2017, ApJ, 847, 33
Casey C. M., Narayanan D., Cooray A., 2014, Phys. Rep., 541, 45
Chen C.-C. et al., 2017, ApJ, 846, 108
Chen C.-C. et al., 2022, ApJ, 929, 159
Cibinel A. et al., 2017, MNRAS, 469, 4683
Cicone C., Maiolino R., Aalto S., Muller S., Feruglio C., 2020, A&A, 633, A163
Cicone C. et al., 2021, A&A, 654, L8
Coppin K. E. K. et al., 2008, MNRAS, 389, 45
Cormier D. et al., 2018, MNRAS, 475, 3909
da Cunha E. et al., 2013, ApJ, 766, 13
Daddi E. et al., 2015, A&A, 577, A46
Dannerbauer H., Daddi E., Riechers D. A., Walter F., Carilli C. L., Dickinson M., Elbaz D., Morrison G. E., 2009, ApJ, 698, L178
Dannerbauer H., Harrington K., Díaz-Sánchez A., Iglesias-Groth S., Rebolo R., Genova-Santos R. T., Krips M., 2019, AJ, 158, 34
Davis T. A., 2014, MNRAS, 445, 2378
De Cia A., Ledoux C., Petitjean P., Savaglio S., 2018, A&A, 611, A76
de los Reyes M. A. C., Kennicutt Robert C. J., 2019a, ApJ, 872, 16
de los Reyes M. A. C., Kennicutt Robert C. J., 2019b, ApJ, 878, 74
Draine B. T., 2003, ARA&A, 41, 241
Draine B. T., Li A., 2007, ApJ, 657, 810
Draine B. T. et al., 2014, ApJ, 780, 172
Dunne L., Eales S. A., 2001, MNRAS, 327, 697
Dunne L., Maddox S. J., Vlahakis C., Gomez H. L., 2021, MNRAS, 501, 2573
Dunne L., Maddox S. J., Papadopoulos P. P., Ivison R. J., Gomez H. L., 2022, MNRAS, 517, 962
Dye S. et al., 2015, MNRAS, 452, 2258
Dye S. et al., 2018, MNRAS, 476, 4383

Eales S., Lilly S., Webb T., Dunne L., Gear W., Clements D., Yun M., 2000, AJ, 120, 2244
Eales S. et al., 2010, PASP, 122, 499
Egami E. et al., 2018, Publ. Astron. Soc. Aust., 35, e048
Engel H. et al., 2010, ApJ, 724, 233
Falgarone E. et al., 2017, Nature, 548, 430
Falstad N. et al., 2021, A&A, 649, A105
Fixsen D. J., Bennett C. L., Mather J. C., 1999, ApJ, 526, 207
Fraternali F., Karim A., Magnelli B., Gómez-Guijarro C., Jiménez-Andrade E. F., Posses A. C., 2021, A&A, 647, A194
Fu H. et al., 2013, Nature, 498, 338
Fudamoto Y. et al., 2017, MNRAS, 472, 2028
Fujimoto S. et al., 2019, ApJ, 887, 107
Fujimoto S. et al., 2020, ApJ, 900, 1
Galliano F., Dwek E., Chanial P., 2008, ApJ, 672, 214
Gao Y., Solomon P. M., 2004, ApJ, 606, 271
Ginolfi M. et al., 2020, A&A, 633, A90
Glazebrook K. et al., 2017, Nature, 544, 71
Glover S. C. O., Clark P. C., Micic M., Molina F., 2015, MNRAS, 448, 1607
Goldsmith P. F., Kauffmann J., 2017, ApJ, 841, 25
González-Alfonso E. et al., 2010, A&A, 518, L43
González-Alfonso E., Fischer J., Aalto S., Falstad N., 2014, A&A, 567, A91
González-Alfonso E., Fischer J., Goicoechea J. R., Yang C., Pereira-Santaella M., Stewart K. P., 2022, A&A, 666, L3
González-Nuevo J. et al., 2012, ApJ, 749, 65
Granato G. L. et al., 2021, MNRAS, 503, 511
Greve T. R., Papadopoulos P. P., Gao Y., Radford S. J. E., 2009, ApJ, 692, 1432
Greve T. R. et al., 2014, ApJ, 794, 142
Griffin M. J. et al., 2010, A&A, 518, L3
Gullberg B. et al., 2018, ApJ, 859, 12
Gullberg B. et al., 2019, MNRAS, 490, 4956
Habing H. J., 1968, Bull. Astron. Inst. Neth., 19, 421
Hainline L. J., Blain A. W., Smail I., Alexander D. M., Armus L., Chapman S. C., Ivison R. J., 2011, ApJ, 740, 96
Harrington K. C. et al., 2021, ApJ, 908, 95
Hatsukade B., Tamura Y., Iono D., Matsuda Y., Hayashi M., Oguri M., 2015, PASJ, 67, 93
Henkel C., Mauersberger R., 1993, A&A, 274, 730
Henkel C., Downes D., Weiß A., Riechers D., Walter F., 2010, A&A, 516, A111
Herrera-Camus R. et al., 2021, A&A, 649, A31
Hezaveh Y. D., Marrone D. P., Holder G. P., 2012, ApJ, 761, 20
Hickox R. C. et al., 2012, MNRAS, 421, 284
Hodge J. A. et al., 2016, ApJ, 833, 103
Hodge J. A. et al., 2019, ApJ, 876, 130
Hollenbach D. J., Tielens A. G. G. M., 1999, Rev. Mod. Phys., 71, 173
Hopkins P. F., Hernquist L., Cox T. J., Kereš D., 2008, ApJS, 175, 356
Hou K.-C., Aoyama S., Hirashita H., Nagamine K., Shimizu I., 2019, MNRAS, 485, 1727
Hu C.-Y., Zhukovska S., Somerville R. S., Naab T., 2019, MNRAS, 487, 3252
Hughes D. H. et al., 1998, Nature, 394, 241
Ikarashi S. et al., 2015, ApJ, 810, 133
Ikeda M., Oka T., Tatematsu K., Sekimoto Y., Yamamoto S., 2002, ApJS, 139, 467
Israel F. P., 2020, A&A, 635, A131
Israel F. P., Rosenberg M. J. F., van der Werf P., 2015, A&A, 578, A95
Ivison R. J. et al., 2010, A&A, 518, L35
Ivison R. J. et al., 2013, ApJ, 772, 137
Ivison R. J. et al., 2016, ApJ, 832, 78
Izumi T. et al., 2021, ApJ, 914, 36
James A., Dunne L., Eales S., Edmunds M. G., 2002, MNRAS, 335, 753
Jarugula S. et al., 2021, ApJ, 921, 97
Jiao Q., Zhao Y., Zhu M., Lu N., Gao Y., Zhang Z.-Y., 2017, ApJ, 840, L18
Jiménez-Donaire M. J. et al., 2017, ApJ, 836, L29
Jiménez-Donaire M. J. et al., 2019, ApJ, 880, 127
Kaasinen M. et al., 2020, ApJ, 899, 37
Kamenetzky J., Rangwala N., Glenn J., Maloney P. R., Conley A., 2016, ApJ, 829, 93
Kaufman M. J., Wolfire M. G., Hollenbach D. J., Luhman M. L., 1999, ApJ, 527, 795
Kaufman M. J., Wolfire M. G., Hollenbach D. J., 2006, ApJ, 644, 283
Kennicutt R. C., Evans N. J., 2012, ARA&A, 50, 531
Kennicutt Robert C. J., 1989, ApJ, 344, 685
Kennicutt Robert C. J., 1998, ApJ, 498, 541
Kennicutt Robert C. J., De Los Reyes M. A. C., 2021, ApJ, 908, 61
Lapi A. et al., 2011, ApJ, 742, 24
Lee M. Y. et al., 2019, A&A, 628, A113
Lelli F., Di Teodoro E. M., Fraternali F., Man A. W. S., Zhang Z.-Y., De Breuck C., Davis T. A., Maiolino R., 2021, Science, 371, 713
Leroy A. K. et al., 2011, ApJ, 737, 12
Lindberg J. E. et al., 2016, A&A, 587, A15
Liu D., Gao Y., Isaak K., Daddi E., Yang C., Lu N., van der Werf P., 2015, ApJ, 810, L14
Liu L. et al., 2017, ApJ, 846, 5
Lizée T., Vollmer B., Braine J., Gratier P., Bigiel F., 2022, A&A, 663, A152
Lu N. et al., 2017, ApJS, 230, 1
Madau P., Dickinson M., 2014, ARA&A, 52, 415
Madden S. C. et al., 2020, A&A, 643, A141
Maiolino R., Mannucci F., 2019, A&AR, 27, 3
Meijerink R., Spaans M., Israel F. P., 2007, A&A, 461, 793
Meijerink R., Spaans M., Loenen A. F., van der Werf P. P., 2011, A&A, 525, A119
Meijerink R. et al., 2013, ApJ, 762, L16
Méndez-Hernández H. et al., 2020, MNRAS, 497, 2771
Merlin E. et al., 2019, MNRAS, 490, 3309
Meyer R. A. et al., 2022, ApJ, 927, 152
Michiyama T. et al., 2021, ApJS, 257, 28
Narayanan D. et al., 2015, Nature, 525, 496
Nayyeri H. et al., 2016, ApJ, 823, 17
Negrello M., Perrotta F., González-Nuevo J., Silva L., de Zotti G., Granato G. L., Baccigalupi C., Danese L., 2007, MNRAS, 377, 1557
Negrello M. et al., 2010, Science, 330, 800
Negrello M. et al., 2014, MNRAS, 440, 1999
Negrello M. et al., 2017, MNRAS, 465, 3558
Neri R. et al., 2003, ApJ, 597, L113
Neri R. et al., 2020, A&A, 635, A7
Ojha R. et al., 2001, ApJ, 548, 253
Omont A. et al., 2013, A&A, 551, A115
Osman O., Bekki K., Cortese L., 2020, MNRAS, 497, 2002
Oteo I. et al., 2016, ApJ, 827, 34
Oteo I. et al., 2017, ApJ, 850, 170
Pantoni L. et al., 2021, MNRAS, 504, 928
Papadopoulos P. P., Greve T. R., 2004, ApJ, 615, L29
Papadopoulos P. P., Thi W. F., Viti S., 2004, MNRAS, 351, 147
Papadopoulos P. P., Bisbas T. G., Zhang Z.-Y., 2018, MNRAS, 478, 1716
Pearson E. A. et al., 2013, MNRAS, 435, 2753
Péroux C., Howk J. C., 2020, ARA&A, 58, 363
Planck Collaboration XIII, 2016, A&A, 594, A13
Poglitsch A. et al., 2010, A&A, 518, L2
Pound M. W., Wolfire M. G., 2008, in Argyle R. W., Bunclark P. S., Lewis J. R.eds, ASP Conf. Ser. Vol. 394, Astronomical Data Analysis Software and Systems XVII. Astron. Soc. Pac., San Francisco, p. 654
Pound M. W., Wolfire M. G., 2011, Astrophysics Source Code Library, record ascl:1102.022
Rangwala N., Maloney P. R., Glenn J., Wilson C. D., Kamenetzky J., Schirm M. R. P., Spinoglio L., Pereira Santaella M., 2014, ApJ, 788, 147
Rémy-Ruyer A. et al., 2014, A&A, 563, A31
Reuter C. et al., 2020, ApJ, 902, 78
Reuter C. et al., 2022, preprint (arXiv:2210.11671)
Riechers D. A., Walter F., Carilli C. L., Weiss A., Bertoldi F., Menten K. M., Knudsen K. K., Cox P., 2006a, ApJ, 645, L13
Riechers D. A. et al., 2006b, ApJ, 650, 604
Riechers D. A., Weiß A., Walter F., Wagg J., 2010, ApJ, 725, 1032
Riechers D. A. et al., 2013, Nature, 496, 329

Riechers D. A. et al., 2017, ApJ, 850, 1
Riechers D. A. et al., 2020, ApJ, 896, L21
Riechers D. A., Cooray A., Pérez-Fournon I., Neri R., 2021, ApJ, 913, 141
Rizzo F., Vegetti S., Powell D., Fraternali F., McKean J. P., Stacey H. R., White S. D. M., 2020, Nature, 584, 201
Rosenberg M. J. F. et al., 2015, ApJ, 801, 72
Rowan-Robinson M. et al., 2016, MNRAS, 461, 1100
Rybak M. et al., 2022, A&A, 667, A70
Sanders D. B., Soifer B. T., Elias J. H., Madore B. F., Matthews K., Neugebauer G., Scoville N. Z., 1988, ApJ, 325, 74
Schmidt M., 1959, ApJ, 129, 243
Schreiber C. et al., 2018, A&A, 618, A85
Serjeant S., 2012, MNRAS, 424, 2429
Shapley A. E., Cullen F., Dunlop J. S., McLure R. J., Kriek M., Reddy N. A., Sanders R. L., 2020, ApJ, 903, L16
Sharon C. E., Riechers D. A., Hodge J., Carilli C. L., Walter F., Weiß A., Knudsen K. K., Wagg J., 2016, ApJ, 827, 18
Shen X., Hopkins P. F., Faucher-Giguère C.-A., Alexander D. M., Richards G. T., Ross N. P., Hickox R. C., 2020, MNRAS, 495, 3252
Shimajiri Y. et al., 2013, ApJ, 774, L20
Simpson J. M. et al., 2017, ApJ, 844, L10
Sliwa K., Wilson C. D., Aalto S., Privon G. C., 2017, ApJ, 840, L11
Smail I., Ivison R. J., Blain A. W., 1997, ApJ, 490, L5
Sobolev V. V., 1960, Moving Envelopes of Stars, Harvard University Press
Solomon P. M., Downes D., Radford S. J. E., Barrett J. W., 1997, ApJ, 478, 144
Spilker J. S. et al., 2014, ApJ, 785, 149
Spilker J. S., Bezanson R., Marrone D. P., Weiner B. J., Whitaker K. E., Williams C. C., 2016, ApJ, 832, 19
Spilker J. S. et al., 2020a, ApJ, 905, 85
Spilker J. S. et al., 2020b, ApJ, 905, 86
Stach S. M., Swinbank A. M., Smail I., Hilton M., Simpson J. M., Cooke E. A., 2017, ApJ, 849, 154
Straatman C. M. S. et al., 2014, ApJ, 783, L14
Stutzki J., Bensch F., Heithausen A., Ossenkopf V., Zielinsky M., 1998, A&A, 336, 697
Swinbank A. M., Chapman S. C., Smail I., Lindner C., Borys C., Blain A. W., Ivison R. J., Lewis G. F., 2006, MNRAS, 371, 465
Swinbank A. M. et al., 2010, Nature, 464, 733
Tacconi L. J. et al., 2006, ApJ, 640, 228
Tacconi L. J. et al., 2013, ApJ, 768, 74
Tacconi L. J. et al., 2018, ApJ, 853, 179
Tacconi L. J., Genzel R., Sternberg A., 2020, ARA&A, 58, 157
Tamura Y., Oguri M., Iono D., Hatsukade B., Matsuda Y., Hayashi M., 2015, PASJ, 67, 72
Taniguchi A., 2020, astropenguin/ndradex: Bug-fix release, https://doi.org/10.5281/zenodo.4139707
Toft S. et al., 2014, ApJ, 782, 68
Triani D. P., Sinha M., Croton D. J., Pacifici C., Dwek E., 2020, MNRAS, 493, 2490
Triani D. P., Sinha M., Croton D. J., Dwek E., Pacifici C., 2021, MNRAS, 503, 1005
Tunnard R., Greve T. R., 2017, ApJ, 849, 37
Umehata H. et al., 2020, A&A, 640, L8
Urquhart S. A. et al., 2022, MNRAS, 511, 3017
Valentino F. et al., 2020a, A&A, 641, A155
Valentino F. et al., 2020b, ApJ, 890, 24
Valiante E. et al., 2016, MNRAS, 462, 3146
Vallini L., Tielens A. G. G. M., Pallottini A., Gallerani S., Gruppioni C., Carniani S., Pozzi F., Talia M., 2019, MNRAS, 490, 4502
van der Tak F. F. S., Black J. H., Schöier F. L., Jansen D. J., van Dishoeck E. F., 2007, A&A, 468, 627
Venemans B. P., Walter F., Zschaechner L., Decarli R., De Rosa G., Findlay J. R., McMahon R. G., Sutherland W. J., 2016, ApJ, 816, 37
Virtanen P. et al., 2020, Nat. Methods, 17, 261
Walter F., Weiß A., Downes D., Decarli R., Henkel C., 2011, ApJ, 730, 18
Wang M., Chin Y.-N., Henkel C., Whiteoak J. B., Cunningham M., 2009, ApJ, 690, 580
Wang R. et al., 2013, ApJ, 773, 44
Wang T.-M. et al., 2022, A&A, 660, A142
Wardlow J. L. et al., 2013, ApJ, 762, 59
Weiß A., Downes D., Neri R., Walter F., Henkel C., Wilner D. J., Wagg J., Wiklind T., 2007, A&A, 467, 955
Weiß A. et al., 2009, ApJ, 707, 1201
Willott C. J., Bergeron J., Omont A., 2015, ApJ, 801, 123
Wilson T. L., Rood R., 1994, ARA&A, 32, 191
Wolfire M. G., Vallini L., Chevance M., 2022, ARA&A, 60, 247
Xie T., Allen M., Langer W. D., 1995, ApJ, 440, 674
Yang C., Gao Y., Omont A., Liu D., Isaak K. G., Downes D., van der Werf P. P., Lu N., 2013, ApJ, 771, L24
Yang C. et al., 2016, A&A, 595, A80
Yang C. et al., 2017, A&A, 608, A144
Yang C. et al., 2019, A&A, 624, A138
Zabel N. et al., 2022, ApJ, 933, 10
Zavala J. A. et al., 2021, ApJ, 909, 165
Zhang Z.-Y., Papadopoulos P. P., Ivison R. J., Galametz M., Smith M. W. L., Xilouris E. M., 2016, R. Soc. Open Sci., 3, 160025
Zhang Z.-Y., Romano D., Ivison R. J., Papadopoulos P. P., Matteucci F., 2018, Nature, 558, 260

APPENDIX A: ADDITIONAL VELOCITY-INTEGRATED LINE FLUXES AND UPPER LIMITS

We extracted three extra [C I] ($^3P_1$–$^3P_0$), three extra [C I] ($^3P_2$–$^3P_1$), and one extra H_2O (2_{11}–2_{02}) lines on top of the lines reported in Urquhart et al. (2022). Together with these, we list 10 upper limits on line fluxes in Table A1.

Table A1. Additional velocity-integrated line fluxes and 3σ upper limits.

Source ID	Line	$S\delta V$ (Jykms^{-1})
HerBS-28	H_2O (2_{11}–2_{02})	1.4 ± 0.4
HerBS-41	[C I] ($^3P_1$–$^3P_0$)	0.73^a
	[C I] ($^3P_2$–$^3P_1$)	1.3 ± 0.4
	H_2O (2_{11}–2_{02})	1.6^a
HerBS-77	[C I] ($^3P_1$–$^3P_0$)	1.5^a
HerBS-80A	[C I] ($^3P_1$–$^3P_0$)	1.1^a
HerBS-90	[C I] ($^3P_2$–$^3P_1$)	4.0 ± 1.1
HerBS-117	[C I] ($^3P_2$–$^3P_1$)	1.7 ± 0.4
HerBS-121	[C I] ($^3P_1$–$^3P_0$)	0.81^a
	H_2O (2_{11}–2_{02})	1.7^a
HerBS-131B	CO (J = 3–2)	1.1^a
HerBS-159A	[C I] ($^3P_1$–$^3P_0$)	1.0 ± 0.2
HerBS-159B	[C I] ($^3P_1$–$^3P_0$)	0.71^a
HerBS-160	[C I] ($^3P_1$–$^3P_0$)	1.2 ± 0.3
	H_2O (2_{11}–2_{02})	1.4^a
HerBS-200	[C I] ($^3P_1$–$^3P_0$)	2.2 ± 0.6
HerBS-208B	[C I] ($^3P_1$–$^3P_0$)	1.2^a

Note. $^a3\sigma$ upper limits.

Table B1. Scaling relation fits to the lines shown in Fig. 4.

Line	a	b
CO ($J = 2$–1)	0.79 ± 0.04	0.6 ± 0.5
CO ($J = 3$–2)	0.91 ± 0.02	−1.1 ± 0.2
CO ($J = 4$–3)	0.97 ± 0.01	−1.9 ± 0.1
CO ($J = 5$–4)	0.996 ± 0.009	−2.5 ± 0.1
CO ($J = 6$–5)	1.02 ± 0.01	−3.0 ± 0.2
CO ($J = 7$–6)	1.05 ± 0.01	−3.7 ± 0.1
[C I] ($^3P_1$–$^3P_0$)	1.02 ± 0.02	−2.9 ± 0.2
[C I] ($^3P_2$–$^3P_1$)	1.02 ± 0.01	−3.3 ± 0.2

APPENDIX B: SCALING RELATIONS

Table B1 shows the linear regression best-fitting results for the lines shown in Fig. 4 according to the following prescription,

$$\log_{10}\left(L'_{\rm line}\ \left[{\rm K\ km\ s^{-1}\ pc^2}\right]\right) = a\log_{10}\left(L_{\rm IR}\ [{\rm L_\odot}]\right) + b. \quad \text{(B1)}$$

APPENDIX C: SIZE ESTIMATION

Table C1 shows the deconvolved sizes obtained from CASA task IMFIT to Band 4 continuum. IMFIT returns major axis ($\theta_{\rm maj}$) and minor axis ($\theta_{\rm min}$) and we use the radius as $r = \sqrt{\theta_{\rm maj}\theta_{\rm min}}$, which turn the surface area into πr^2. For the 21 sources that are not listed in Table C1, we set the size to the minimum robust results found, equal to 0.14arcseconds.

Table C1. The size estimation from IMFIT result.

Source ID	Size (kpc)	Source ID	Size (kpc)
HerBS-11	2.2 ± 0.2	HerBS-93	3.8 ± 0.5
HerBS-14	4.17 ± 0.06	HerBS-102	2.2 ± 0.7
HerBS-18	3.7 ± 0.2	HerBS-106	3.4 ± 1.2
HerBS-21	3.9 ± 0.2	HerBS-107	4.7 ± 0.1
HerBS-22	3.8 ± 0.2	HerBS-111	4.4 ± 0.3
HerBS-24	1.1 ± 0.8	HerBS-117	3.1 ± 0.1
HerBS-25	6.9 ± 0.9	HerBS-120B	3.8 ± 0.4
HerBS-27	2.8 ± 0.5	HerBS-121	5.7 ± 0.2
HerBS-28	5.0 ± 0.1	HerBS-123	9.0 ± 1.1
HerBS-37	5.6 ± 0.3	HerBS-131B	2.6 ± 0.7
HerBS-39	6.8 ± 0.4	HerBS-132	3.2 ± 0.2
HerBS-41	2.0 ± 0.6	HerBS-135A	3.0 ± 0.8
HerBS-42	2.3 ± 0.4	HerBS-145	4.5 ± 0.5
HerBS-47	5.2 ± 0.2	HerBS-146B	5.5 ± 0.7
HerBS-49A	6.8 ± 0.2	HerBS-155	5.4 ± 0.6
HerBS-55	5.1 ± 0.2	HerBS-159A	8.8 ± 1.6
HerBS-57	3.8 ± 0.4	HerBS-160	3.7 ± 0.1
HerBS-60	5.0 ± 0.3	HerBS-168	5.2 ± 0.4
HerBS-63	2.5 ± 0.7	HerBS-178A	4.3 ± 0.2
HerBS-69A	2.2 ± 1.1	HerBS-178B	5.4 ± 0.8
HerBS-73	2.0 ± 0.5	HerBS-182	1.2 ± 0.4
HerBS-77	3.1 ± 3.2	HerBS-189	6.4 ± 0.9
HerBS-80B	4.7 ± 0.3	HerBS-207	3.5 ± 0.7
HerBS-86	3.0 ± 0.5	HerBS-208A	2.7 ± 0.9
HerBS-90	4.6 ± 1.0	HerBS-209	6.7 ± 2.5

APPENDIX D: DERIVED PROPERTIES OF THE BEARS SAMPLE

We list the galaxy properties derived througout this paper in Table D1.

Table D1. Derived properties of the BEARS sample.

ID	$\mu L_{\rm IR}$ (10^{12} L$_\odot$)	$\mu M_{\rm dust}$ (10^{10} M$_\odot$)	$\mu L'_{\rm CO(1-0)}$ (10^{10} K kms^{-1} pc^2)	$\mu M_{\rm H_2(CI)}$ (10^{11} M$_\odot$)	$\mu M_{\rm H_2(CO)}$ (10^{11} M$_\odot$)	$M_{\rm dyn}$ (10^{11} M$_\odot$)	$\Sigma_{\rm M_{H_2}(CI)}$ (10^4 M$_\odot$ pc^{-2})	$\Sigma_{\rm M_{H_2}(CO)}$ (10^4 M$_\odot$ pc^{-2})	$\Sigma_{\rm SFR}$ (10^2 M$_\odot$ yr^{-1} kpc^{-2})
11	66.4	13.6	58.9 ± 10.9	–	23.6 ± 4.4	1.5 ± 0.3	–	15.9 ± 3.0	6.6 ± 1.7
14	97.8	20.1	52.9 ± 14.5	11.8 ± 1.7	21.2 ± 5.8	1.4 ± 0.3	2.2 ± 0.3	3.9 ± 1.1	2.6 ± 0.7
18	58.0	11.9	40.7 ± 11.5	9.7 ± 1.1	16.3 ± 4.6	0.9 ± 0.3	2.4 ± 0.3	3.1 ± 0.6	2.1 ± 0.5
21	45.8	9.4	76.1 ± 43.5	–	30.4 ± 17.4	4.9 ± 2.2	–	3.1 ± 0.9	1.4 ± 0.4
22	50.8	10.4	61.3 ± 25.4	–	24.5 ± 10.2	7.5 ± 3.7	–	5.3 ± 2.2	1.6 ± 0.4
24	56.7	11.6	20.9 ± 4.0	11.4 ± 1.6	8.3 ± 1.6	1.1 ± 0.3	27.7 ± 3.9	20.3 ± 3.8	20.2 ± 5.1
25	59.8	12.3	78.2 ± 33.1	–	31.3 ± 13.2	1.3 ± 0.5	–	1.1 ± 0.2	0.6 ± 0.1
27	98.6	20.2	79.7 ± 32.7	–	31.9 ± 13.1	2.7 ± 1.0	–	13.1 ± 5.4	6.0 ± 1.5
28	71.8	14.7	85.2 ± 51.5	–	34.1 ± 20.6	7.5 ± 2.7	–	2.1 ± 0.7	1.4 ± 0.3
36	77.5	15.9	23.6 ± 6.9	–	9.4 ± 2.7	1.2 ± 0.3	–	25.1 ± 7.3	30.3 ± 7.6
37	29.7	6.1	34.7 ± 16.7	–	13.9 ± 6.7	4.8 ± 2.1	–	0.8 ± 0.2	0.4 ± 0.1
39	46.7	9.6	33.7 ± 9.7	–	13.5 ± 3.9	9.3 ± 5.9	–	0.9 ± 0.3	0.5 ± 0.1
40	22.0	4.5	16.2 ± 4.5	–	6.5 ± 1.8	2.6 ± 0.6	–	14.3 ± 4.0	7.1 ± 1.8
41	47.1	9.7	18.9 ± 6.0	4.6[a]	7.5 ± 2.4	2.6 ± 0.7	3.5[a]	5.7 ± 1.8	5.3 ± 1.3
42	27.8	5.7	38.9 ± 23.9	–	15.6 ± 9.5	4.0 ± 0.9	–	4.4 ± 1.6	2.4 ± 0.6
45	13.2	2.7	10.8 ± 2.7	8.1 ± 1.4	4.3 ± 1.1	0.2 ± 0.1	19.1 ± 3.2	10.1 ± 2.5	4.5 ± 1.1
47	25.0	5.1	21.6 ± 8.4	4.3 ± 0.8	8.6 ± 3.4	6.9 ± 3.6	0.5 ± 0.1	1.0 ± 0.4	0.4 ± 0.1
49A	21.6	4.4	37.1 ± 19.0	–	14.8 ± 7.6	1.0 ± 0.2	–	0.6 ± 0.2	0.2 ± 0.1
49B	8.8	1.8	8.4 ± 3.7	–	3.4 ± 1.5	1.1 ± 0.5	–	8.3 ± 3.7	3.2 ± 0.8
55	19.3	4.0	16.3 ± 3.6	–	6.5 ± 1.4	1.8 ± 0.6	–	0.8 ± 0.2	0.3 ± 0.1
56C	6.6	1.4	10.2 ± 2.4	–	4.1 ± 0.9	0.5 ± 0.2	–	9.8 ± 2.3	2.3 ± 0.6
57	46.8	9.6	36.6 ± 10.4	–	14.7 ± 4.2	1.3 ± 0.4	–	3.2 ± 0.9	1.5 ± 0.4
60	39.0	8.0	27.4 ± 7.9	–	11.0 ± 3.2	3.1 ± 1.6	–	1.4 ± 0.4	0.7 ± 0.2
63	21.0	4.3	9.9 ± 2.2	5.4 ± 0.8	3.9 ± 0.9	1.7 ± 0.5	2.8 ± 0.4	2.0 ± 0.5	1.6 ± 0.4
68	29.2	6.0	68.7 ± 29.1	–	27.5 ± 11.6	0.9 ± 0.3	–	36.4 ± 7.7	10.6 ± 2.6
69A	15.2	3.1	19.5 ± 4.0	6.2 ± 0.6	7.8 ± 1.6	1.3 ± 0.5	4.2 ± 0.4	5.3 ± 1.1	1.5 ± 0.4
69B	12.1	2.5	2.1 ± 0.8	1.4 ± 0.4	0.9 ± 0.3	0.08 ± 0.01	3.2 ± 0.9	1.9 ± 0.7	4.0 ± 1.0
73	34.3	7.0	26.3 ± 11.0	–	10.5 ± 4.4	3.3 ± 1.6	–	8.7 ± 3.6	4.2 ± 1.0
77	22.4	4.6	22.2 ± 4.3	3.6[a]	8.9 ± 1.7	5.1 ± 1.4	1.2[a]	3.0 ± 0.6	1.1 ± 0.3
80A	6.3	1.3	14.5 ± 3.5	2.6[a]	5.8 ± 1.4	2.1 ± 0.2	6.0[a]	13.2 ± 3.2	2.1 ± 0.5
80B	6.4	1.3	4.1 ± 1.3	–	1.6 ± 0.5	2.3 ± 1.0	–	0.2 ± 0.1	0.1 ± 0.0
81A	11.4	2.3	27.7 ± 8.6	–	11.1 ± 3.4	2.1 ± 1.4	–	29.8 ± 9.3	4.5 ± 1.1
81B	12.4	2.5	9.4 ± 2.3	–	3.7 ± 0.9	3.0 ± 1.1	–	9.0 ± 2.2	4.4 ± 1.1
86c	29.5	6.0	28.7 ± 5.6	–	11.5 ± 2.2	3.2 ± 1.0	–	4.1 ± 0.8	1.5 ± 0.4
90	41.3	8.5	26.1 ± 8.1	25.1 ± 6.1	10.4 ± 3.2	2.2 ± 0.8	3.8 ± 0.9	1.6 ± 0.5	0.9 ± 0.2
93	27.6	5.7	18.8 ± 4.6	7.2 ± 1.3	7.5 ± 1.8	6.5 ± 3.7	1.6 ± 0.3	1.7 ± 0.4	0.9 ± 0.2
102	21.1	4.3	21.4 ± 6.7	–	8.6 ± 2.7	1.1 ± 0.6	–	5.6 ± 1.8	2.0 ± 0.5
103	23.6	4.8	30.9 ± 12.7	–	12.3 ± 5.1	1.6 ± 0.8	–	31.8 ± 13.1	8.9 ± 2.2
106	29.7	6.1	18.8 ± 4.0	4.4 ± 0.8	7.5 ± 1.6	3.6 ± 2.9	1.2 ± 0.2	2.1 ± 0.4	1.2 ± 0.3
107	18.9	3.9	16.8 ± 3.6	–	6.7 ± 1.4	0.8 ± 0.3	–	1.0 ± 0.2	0.4 ± 0.1
111	22.7	4.6	29.6 ± 6.0	7.5 ± 0.8	11.9 ± 2.4	6.7 ± 2.9	1.2 ± 0.1	2.0 ± 0.4	0.6 ± 0.1
117	39.8	8.2	25.9 ± 11.0	–	10.4 ± 4.4	2.5 ± 0.8	–	3.3 ± 1.4	1.9 ± 0.5
120A	18.5	3.8	10.7 ± 4.3	–	4.3 ± 1.7	2.0 ± 0.8	–	11.4 ± 4.6	7.3 ± 1.8
120B	18.2	3.7	6.7 ± 3.1	–	2.7 ± 1.2	8.9 ± 5.1	–	0.4 ± 0.1	0.6 ± 0.1
121	27.0	5.5	32.8 ± 10.1	4.5[a]	13.1 ± 4.1	3.3 ± 1.0	0.4[a]	1.3 ± 0.4	0.4 ± 0.1
122A	6.3	1.3	13.9 ± 5.8	–	5.5 ± 2.3	0.6 ± 0.3	–	14.1 ± 5.9	2.4 ± 0.6
123	22.4	4.6	22.7 ± 4.6	10.3 ± 1.3	9.1 ± 1.8	3.5 ± 1.3	0.4 ± 0.1	0.4 ± 0.1	0.13 ± 0.03
131B	15.7	3.2	5.9 ± 1.8	10.3 ± 0.9	2.4 ± 0.7	6.2 ± 2.3	4.8 ± 0.4	0.8 ± 0.2	1.1 ± 0.3
132	16.7	3.4	19.3 ± 4.1	3.4 ± 0.6	7.7 ± 1.7	2.8 ± 1.4	1.1 ± 0.2	2.5 ± 0.5	0.8 ± 0.2
135A	17.1	3.5	12.4 ± 3.1	2.9 ± 0.5	5.0 ± 1.3	1.8 ± 0.6	1.1 ± 0.2	1.8 ± 0.5	0.9 ± 0.2
138B	23.6	4.8	3.7 ± 0.7	–	1.5 ± 0.3	0.07 ± 0.02	–	3.2 ± 0.6	7.5 ± 1.9
141	16.0	3.3	20.8 ± 5.1	10.6 ± 1.7	8.3 ± 2.0	0.6 ± 0.2	23.6 ± 3.7	18.5 ± 4.5	5.2 ± 1.3
145	13.8	2.8	19.9 ± 4.5	–	8.0 ± 1.8	8.2 ± 2.0	–	1.2 ± 0.3	0.3 ± 0.1
146B	8.8	1.8	10.7 ± 3.1	–	4.3 ± 1.3	3.7 ± 1.6	–	0.5 ± 0.1	0.14 ± 0.03
155	34.7	7.1	21.0 ± 8.6	–	8.4 ± 3.5	0.7 ± 0.4	–	0.9 ± 0.4	0.5 ± 0.1
159A	14.0	2.9	19.1 ± 3.7	2.3 ± 0.5	7.6 ± 1.5	1.6 ± 0.7	0.10 ± 0.02	0.3 ± 0.1	0.08 ± 0.02
159B	4.8	1.0	3.2 ± 0.9	1.7[a]	1.3 ± 0.3	0.6 ± 0.2	3.8[a]	2.9 ± 0.8	1.6 ± 0.4
160	50.5	10.4	19.4 ± 6.1	7.2 ± 1.8	7.8 ± 2.4	2.9 ± 0.7	1.7 ± 0.4	1.8 ± 0.6	1.7 ± 0.4
163A	6.5	1.3	4.3 ± 1.6	–	1.7 ± 0.6	0.7 ± 0.3	–	4.6 ± 1.7	2.6 ± 0.6
168	49.2	10.1	17.1 ± 3.6	–	6.9 ± 1.5	11.1 ± 3.0	–	0.8 ± 0.2	0.9 ± 0.2
178A	14.1	2.9	16.4 ± 3.3	–	6.5 ± 1.3	5.0 ± 2.2	–	1.1 ± 0.2	0.4 ± 0.1

Table D1 – *continued*

ID	$\mu L_{\rm IR}$ (10^{12} L$_\odot$)	$\mu M_{\rm dust}$ (10^{10} M$_\odot$)	$\mu L'_{\rm CO(1-0)}$ (10^{10} K kms^{-1} pc^2)	$\mu M_{\rm H_2(CI)}$ (10^{11} M$_\odot$)	$\mu M_{\rm H_2(CO)}$ (10^{11} M$_\odot$)	$M_{\rm dyn}$ (10^{11} M$_\odot$)	$\Sigma_{\rm M_{H_2}(CI)}$ (10^4 M$_\odot$ pc^{-2})	$\Sigma_{\rm M_{H_2}(CO)}$ (10^4 M$_\odot$ pc^{-2})	$\Sigma_{\rm SFR}$ (10^2 M$_\odot$ yr^{-1} kpc^{-2})
178B	9.9	2.0	14.2 ± 3.0	–	5.7 ± 1.2	8.2 ± 2.7	–	0.6 ± 0.1	0.16 ± 0.04
178C	6.2	1.3	7.6 ± 2.1	–	3.0 ± 0.8	0.6 ± 0.3	–	7.4 ± 2.1	2.2 ± 0.6
182	21.8	4.5	15.7 ± 3.9	7.2 ± 1.2	6.3 ± 1.6	3.8 ± 1.1	15.7 ± 2.5	13.7 ± 3.4	7.0 ± 1.7
184	28.6	5.9	21.6 ± 6.1	6.0 ± 0.9	8.7 ± 2.5	0.5 ± 0.2	14.3 ± 2.0	20.6 ± 5.8	10.0 ± 2.5
189	29.0	6.0	27.4 ± 7.9	–	10.9 ± 3.2	2.6 ± 0.9	–	0.8 ± 0.2	0.3 ± 0.1
200	16.7	3.4	11.4 ± 2.7	4.8 ± 1.3	4.6 ± 1.1	0.8 ± 0.4	10.8 ± 3.0	10.2 ± 2.5	5.5 ± 1.4
207	22.5	4.6	26.5 ± 3.1	–	10.6 ± 1.2	3.2 ± 1.0	–	2.7 ± 0.3	0.8 ± 0.2
208A	15.7	3.2	17.0 ± 4.5	5.6 ± 0.8	6.8 ± 1.8	6.9 ± 2.7	2.4 ± 0.4	2.9 ± 0.8	1.0 ± 0.2
208B	10.8	2.2	11.7 ± 2.8	3.4[a]	4.7 ± 1.1	2.5 ± 1.3	8.0[a]	11.0 ± 2.7	3.8 ± 0.9
209	13.6	2.8	10.8 ± 2.5	–	4.3 ± 1.0	6.6 ± 0.8	–	0.3 ± 0.1	0.14 ± 0.04

Note. [a]Calculated from 3σ upper limits shown in Table A1.

APPENDIX E: WHY DIFFERENTIAL LENSING OR A MULTPHASE ISM CANNOT PRODUCE SUPERTHERMALIZED LINE PROFILES

Here, to see why differential magnification nor multiphase ISMs cannot create super-thermalized lines, we consider the following toy model. We suppose the case that there are two CO transitions, $J =$ 4–3 and $J =$ 3–2. For thermalized lines, we can write $L'_{\rm CO(4-3)} = L'_{\rm CO(3-2)}$. For thermalized or sub-thermalized lines in a single-phase ISM region, we can generalize this to $L'_{\rm CO(4-3)} = kL'_{\rm CO(3-2)}$ where the constant $0 < k \leq 1$, with $k = 1$ meaning it is thermalized.

Now suppose that there is some variation in k across the galaxy, perhaps due to the multiphase ISM, so we split the galaxy into N discrete regions, labelled $i = 1$ to $i = N$. Each region has a thermalization coefficient, k_i. In other words, for each region

$$L'_{i\rm CO(4-3)} = k_i L'_{i\rm CO(3-2)}. \tag{E1}$$

Now we assume that this galaxy also has differential magnification, with each region being magnified by a factor of $|\mu_i|$. We can set every $|\mu_i|$ to be $|\mu_i| \geq 1$ (though formally our toy model only requires having at least one non-zero $|\mu_i|$). The total observed CO ($J =$ 4–3) line luminosity will be

$$\begin{aligned} L'_{\rm obs CO(4-3)} &= \sum_{i=1}^{N} |\mu_i| L'_{i\rm CO(4-3)} \\ &= \sum_{i=1}^{N} |\mu_i| k_i L'_{i\rm CO(3-2)}. \end{aligned} \tag{E2}$$

Meanwhile, the total observed CO ($J =$ 3–2) will be

$$L'_{\rm obs CO(3-2)} = \sum_{i=1}^{N} |\mu_i| L'_{i\rm CO(3-2)}. \tag{E3}$$

If we take the ratio of these two observed line luminosities, we obtain an 'effective' observed total k for the differentially magnified galaxy:

$$\begin{aligned} k_{\rm obs} &= \frac{L'_{\rm obs CO(4-3)}}{L'_{\rm obs CO(3-2)}} \\ &= \frac{\sum_{i=1}^{N} |\mu_i| k_i L'_{i\rm CO(3-2)}}{\sum_{i=1}^{N} |\mu_i| L'_{i\rm CO(3-2)}} \end{aligned} \tag{E4}$$

where we have used equation (E2). However, every $k_i \leq 1$, which means that every term in the numerator will be smaller than or equal to the corresponding term in the denominator. Therefore, $k_{\rm obs}$ is necessarily $k_{\rm obs} \leq 1$. Therefore, no amount of differential magnification nor combination of regions with different ISM phases can create a super-thermalized line ratio ($k_{\rm obs} > 1$) from individual thermalized or sub-thermalized components with each individual $k_i \leq 1$.

APPENDIX F: STACKED SPECTRUM LINE LUMINOSITIES

We report the line luminosities of the stacked spectrum in Table F1.

Table F1. Spectral line luminosities from the stacked spectrum.

Line	Frequency (GHz)	Sources	Line luminosity (10^9 K kms^{-1} pc^2)	S/N	Line	Frequency (GHz)	Sources	Line luminosity (10^9 K kms^{-1} pc^2)	S/N
CO (2–1)	230.5380	2	**129.3 ± 14.9**	(9.9σ)	H_2O^+ 607	607.2273	20	− 0.1 ± 1.1	(−0.1σ)
CO (3–2)	345.7960	42	**98.1 ± 6.1**	(37.9σ)	H_2O^+ 631	631.7241	17	− 0.6 ± 1.0	(−0.5σ)
CO (4–3)	461.0408	35	**74.2 ± 4.4**	(53.8σ)	H_2O^+ 634	634.2729	17	− 0.8 ± 1.1	(−0.7σ)
CO (5–4)	576.2679	27	**69.4 ± 4.0**	(68.0σ)	H_2O^+ 721	721.9274	6	− 2.5 ± 1.5	(−1.7σ)
CO (6–5)	691.4731	10	**50.5 ± 3.1**	(40.1σ)	H_2O^+ 742	742.1090	5	1.4 ± 1.5	(1.0σ)
CO (7–6)	806.8984	4	**38.2 ± 2.6**	(25.6σ)	H_2O^+ 746	746.5417	5	**5.0 ± 1.4**	(3.8σ)
^{13}CO (2–1)	220.3987	1	7.3 ± 18.4	(0.4σ)	H_2O^+ 761	761.8188	6	0.2 ± 1.2	(0.2σ)
^{13}CO (3–2)	330.5880	41	4.3 ± 3.2	(1.4σ)	LiH (1–0)	443.9529	30	− 2.4 ± 1.7	(−1.5σ)
^{13}CO (4–3)	440.7652	28	2.2 ± 2.0	(1.1σ)	CH 532	532.7239	34	**6.8 ± 1.2**	(5.8σ)
^{13}CO (5–4)	550.9263	29	1.6 ± 1.2	(1.4σ)	CH 536	536.7614	31	**7.8 ± 1.3**	(6.5σ)
^{13}CO (6–5)	661.0673	14	1.2 ± 1.2	(1.0σ)	OH 425	425.0363	25	0.4 ± 2.5	(0.2σ)
^{13}CO (7–6)	771.1841	7	−0.9 ± 1.0	(−0.9σ)	OH 446	446.2910	31	2.5 ± 1.5	(1.6σ)
^{13}CO (8–7)	881.2728	2	−1.2 ± 1.5	(−0.8σ)	CN (N = 3–2)	340.2478	41	2.1 ± 2.8	(0.8σ)
$C^{18}O$ (2–1)	219.5603	1	−24.3 ± 19.8	(−1.2σ)	CN (N = 4–3)	453.6067	36	2.2 ± 1.4	(1.6σ)
$C^{18}O$ (3–2)	329.3305	42	2.7 ± 3.2	(0.9σ)	CN (N = 5–4)	566.9470	26	0.8 ± 1.1	(0.7σ)
$C^{18}O$ (4–3)	439.0888	27	−0.2 ± 2.0	(−0.1σ)	CN (N = 6–5)	680.2641	9	0.4 ± 1.3	(0.3σ)
$C^{18}O$ (5–4)	548.8310	33	2.0 ± 1.1	(1.8σ)	SiO (7–6)	303.9270	19	5.3 ± 4.9	(1.1σ)
$C^{18}O$ (6–5)	658.5533	14	1.0 ± 1.2	(0.9σ)	SiO (8–7)	347.3306	38	− 1.7 ± 2.6	(−0.7σ)
$C^{18}O$ (7–6)	768.2515	7	0.8 ± 1.1	(0.7σ)	SiO (9–8)	390.7284	40	0.3 ± 2.3	(0.1σ)
$C^{18}O$ (8–7)	877.9219	2	−1.0 ± 1.6	(−0.7σ)	SiO (10–9)	434.1196	25	1.2 ± 2.2	(0.6σ)
[C I] ($^3P_1$–$^3P_0$)	492.1606	32	**29.0 ± 2.1**	(23.0σ)	SiO (11–10)	477.5031	35	− 1.0 ± 1.3	(−0.8σ)
[C I] ($^3P_2$–$^3P_1$)	809.3419	4	**18.8 ± 1.8**	(12.4σ)	SiO (12–11)	520.8782	40	1.2 ± 1.2	(1.0σ)
HCN (3–2)	265.8864	3	0.2 ± 9.2	(0.0σ)	SiO (13–12)	564.2440	27	− 0.8 ± 1.1	(−0.7σ)
HCN (4–3)	354.5055	40	**7.6 ± 2.6**	(3.0σ)	SiO (14–13)	607.5994	20	− 0.5 ± 1.1	(−0.4σ)
HCN (5–4)	443.1161	29	3.0 ± 1.7	(1.8σ)	SiO (15–14)	650.9436	14	− 0.4 ± 1.1	(−0.4σ)
HCN (6–5)	531.7164	34	4.4 ± 1.2	(3.8σ)	SiO (16–15)	694.2754	9	0.3 ± 1.3	(0.2σ)
HCN (7–6)	620.3040	20	1.4 ± 1.1	(1.4σ)	SiO (17–16)	737.5939	6	0.1 ± 1.3	(0.1σ)
HCN (8–7)	708.8770	6	0.8 ± 1.4	(0.5σ)	CS (6–5)	293.9122	17	− 10.7 ± 5.8	(−1.9σ)
HCN (9–8)	797.4333	6	−1.0 ± 1.2	(−0.9σ)	CS (7–6)	342.8830	42	3.5 ± 2.7	(1.3σ)
HCN (10–9)	885.9707	2	−2.2 ± 1.5	(−1.5σ)	CS (8–7)	391.8470	39	− 0.2 ± 2.3	(−0.1σ)
HNC (3–2)	271.9811	4	8.7 ± 11.2	(0.8σ)	CS (10–9)	489.7510	33	1.0 ± 1.3	(0.8σ)
HNC (4–3)	362.6303	35	0.3 ± 3.0	(0.1σ)	CS (11–10)	538.6888	33	− 0.2 ± 1.2	(−0.1σ)
HNC (5–4)	453.2699	36	3.4 ± 1.4	(2.4σ)	CS (12–11)	587.6162	23	1.0 ± 1.1	(0.9σ)
HNC (6–5)	543.8976	34	1.8 ± 1.2	(1.6σ)	CS (13–12)	636.5318	15	− 0.6 ± 1.2	(−0.5σ)
HNC (7–6)	634.5108	17	0.4 ± 1.1	(0.3σ)	CS (14–13)	685.4348	10	1.0 ± 1.2	(0.8σ)
HNC (8–7)	725.1073	6	−0.3 ± 1.3	(−0.2σ)	CS (15–14)	734.3240	6	0.8 ± 1.3	(0.6σ)
HNC (9–8)	815.6847	3	−1.1 ± 1.6	(−0.7σ)	NH_3 (1_0–0_0)	572.4982	25	1.0 ± 1.0	(1.0σ)
HCO^+ (3–2)	267.5576	4	5.1 ± 8.3	(0.6σ)	N_2H^+ (3–2)	279.5117	8	1.4 ± 9.0	(0.2σ)
HCO^+ (4–3)	356.7342	40	3.4 ± 2.5	(1.4σ)	N_2H^+ (4–3)	372.6725	39	− 1.6 ± 2.3	(−0.7σ)
HCO^+ (5–4)	445.9029	31	4.5 ± 1.5	(3.0σ)	N_2H^+ (5–4)	465.8250	32	0.1 ± 1.5	(0.1σ)
HCO^+ (6–5)	535.0616	33	1.6 ± 1.2	(1.3σ)	N_2H^+ (6–5)	558.9667	27	− 2.1 ± 1.3	(−1.7σ)
HCO^+ (7–6)	624.2085	17	0.6 ± 1.1	(0.5σ)	N_2H^+ (7–6)	652.0959	15	− 0.8 ± 1.1	(−0.7σ)
HCO^+ (8–7)	713.3414	5	0.1 ± 1.4	(0.0σ)	N_2H^+ (8–7)	745.2103	6	1.9 ± 1.3	(1.5σ)
HCO^+ (9–8)	802.4582	5	−2.5 ± 1.4	(−1.9σ)	CCH (3–2)	262.0042	2	1.0 ± 9.4	(0.1σ)
HCO^+ (10–9)	891.5573	2	−0.6 ± 1.5	(−0.4σ)	CCH (4–3)	349.3387	40	1.1 ± 2.6	(0.4σ)
HOC^+ (3–2)	268.4510	4	−1.4 ± 8.5	(−0.2σ)	CCH (5–4)	436.6604	27	− 4.0 ± 2.1	(−1.9σ)
HOC^+ (4–3)	357.9219	40	−5.0 ± 2.4	(−2.1σ)	CCH (6–5)	523.9704	37	− 0.9 ± 1.2	(−0.7σ)
HOC^+ (5–4)	447.3818	30	−0.7 ± 1.5	(−0.5σ)	CCH (7–6)	611.2650	20	− 0.1 ± 1.1	(−0.1σ)
HOC^+ (6–5)	536.8279	31	7.6 ± 1.3	(6.4σ)	CCH (8–7)	698.5416	7	0.3 ± 1.4	(0.2σ)
HOC^+ (7–6)	626.2575	17	−0.0 ± 1.1	(−0.0σ)	H21α	662.4042	13	0.7 ± 1.2	(0.6σ)
HOC^+ (8–7)	715.6679	6	0.3 ± 1.4	(0.2σ)	H22α	577.8964	27	0.3 ± 1.0	(0.3σ)
HOC^+ (9–8)	805.0563	4	0.7 ± 1.5	(0.5σ)	H23α	507.1755	35	− 0.8 ± 1.1	(−0.8σ)
H_2O ($5_{1,5}$–$4_{2,2}$)	325.1529	38	−5.8 ± 3.4	(−1.7σ)	H24α	447.5403	30	0.1 ± 1.5	(0.0σ)
H_2O ($4_{1,4}$–$3_{2,1}$)	380.1974	42	0.7 ± 2.2	(0.3σ)	H25α	396.9008	35	− 1.6 ± 2.4	(−0.7σ)
H_2O ($4_{2,3}$–$3_{3,0}$)	448.0011	31	1.8 ± 1.5	(1.2σ)	H26α	353.6227	41	5.2 ± 2.5	(2.1σ)
H_2O ($5_{3,3}$–$4_{4,0}$)	474.6891	33	−2.2 ± 1.3	(−1.6σ)	H27α	316.4154	29	− 4.7 ± 4.0	(−1.2σ)
H_2O ($1_{1,0}$–$1_{0,1}$)	556.9360	30	−1.0 ± 1.2	(−0.8σ)	H28α	284.2506	10	9.0 ± 8.0	(1.1σ)
H_2O ($2_{1,1}$–$2_{0,2}$)	752.0331	5	**10.6 ± 1.4**	(8.5σ)	CH^+	835.0789	2	− 0.5 ± 1.7	(−0.3σ)
H_2O^+ 604	604.6786	22	0.6 ± 1.1	(0.6σ)					

Note. Lines in boldface indicate >3σ detections. Note that the apparent HCN (6–5) and HOC^+ (6–5) 'detections' are due to line confusion with CH 532 and 536.

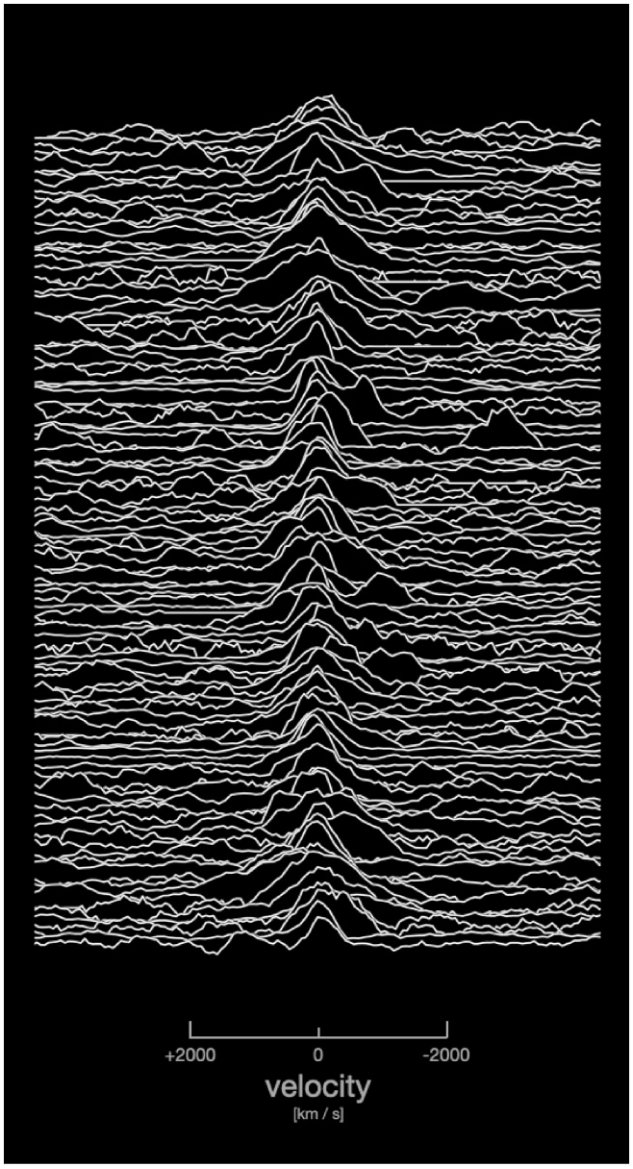

Figure G1. Demonstration of the diversity of the CO and [C I] ($^3P_1$–$^3P_0$) line profiles in the BEARS data set, visualized by superposing them with slight offsets, i.e. the vertical axis is linear in flux, scaled to the peak flux density value of each line. The horizontal axis shows the line velocity. Note the striking variation in widths and shapes, which we have found is not as obviously apparent in other visualizations of the data. For plotting purposes, we exclude any sources within 4000 km s^{-1} of the edge of the spectral windows. The line profiles are stacked in no particular order.

APPENDIX G: DIVERSITY IN THE LINE PROFILES

Fig. G1 graphically demonstrates the diversity in line profiles across the BEARS systems.

[1]*Department of Physics, Graduate School of Science, Nagoya University, Nagoya, Aichi 464-8602, Japan*
[2]*National Astronomical Observatory of Japan, 2-21-1, Osawa, Mitaka, Tokyo 181-8588, Japan*
[3]*School of Physical Sciences, The Open University, Milton Keynes MK7 6AA, UK*
[4]*UK ALMA Regional Centre Node, Jodrell Bank Centre for Astrophysics, Department of Physics and Astronomy, University of Manchester, Oxford Road, Manchester M13 9PL, UK*
[5]*School of Physics and Astronomy, Cardiff University, The Parade, Cardiff CF24 3AA, UK*
[6]*European Southern Observatory, Alonso de Córdova 3107, Vitacura, Casilla 19001, Santiago de Chile, Chile*
[7]*Institute for Advanced Research, Nagoya University, Furocho, Chikusa, Nagoya 464-8602, Japan*
[8]*Institut de Radioastronomie Millimétrique (IRAM), 300 Rue de la Piscine, F-38400 Saint-Martin-d'Hères, France*
[9]*Department of Physics & Astronomy, University of California, Irvine, 4129 Reines Hall, Irvine, CA 92697, USA*
[10]*Institut d'Astrophysique de Paris, Sorbonne Université,UPMC Université Paris 6 and CNRS, UMR 7095, 98 bis boulevard Arago, F-75014 Paris, France*
[11]*INAF – Osservatorio Astronomico di Padova, Vicolo dell'Osservatorio 5, I-35122 Padova, Italy*
[12]*Centre de Recherche Astrophysique de Lyon, ENS de Lyon, Université Lyon 1, CNRS, UMR5574, F-69230 Saint-Genis-Laval, France*
[13]*I. Physikalisches Institut, Universität zu Köln, Zülpicher Strasse 77, D-50937 Köln, Germany*
[14]*Department of Physics and Astronomy, University of British Columbia, 6224 Agricultural Road, Vancouver, BC V6T 1Z1, Canada*
[15]*Astrophysics Branch, NASA–Ames Research Center, MS 245-6, Moffett Field, CA 94035, USA*
[16]*Leiden Observatory, Leiden University, PO Box 9513, NL-2300 RA Leiden, the Netherlands*
[17]*Department of Earth and Space Sciences, Chalmers University of Technology, Onsala Observatory, SE-439 94 Onsala, Sweden*
[18]*Department of Physics, Centre for Extragalactic Astronomy, Durham University, South Road, Durham DH1 3LE, UK*
[19]*European Southern Observatory, Karl Schwarzschild Strasse 2, D-85748 Garching, Germany*
[20]*Department of Physics and Astronomy, Rutgers, the State University of New Jersey, 136 Frelinghuysen Road, Piscataway, NJ 08854-8019, USA*
[21]*Department of Physics and Astronomy, University of the Western Cape, Robert Sobukwe Road, Bellville 7535, South Africa*
[22]*Dipartimento di Fisica e Astronomia 'G. Galilei', Universit'di Padova, Vicolo dell'Osservatorio 3, I-35122 Padova, Italy*
[23]*Aix-Mar seille Univer sitè, CNRS and CNES, Laboratoire d'Astrophysique de Marseille, 38, rue Frèdèric Joliot-Curie, F-13388 Marseille, France*
[24]*Instituto Astrofísica de Canarias (IAC), E-38205 La Laguna, Tenerife, Spain*
[25]*Departomento de Astrofísica, Universidad de La Laguna, E-38206 La Laguna, Tenerife, Spain*
[26]*School of Physics & Astronomy, University of Nottingham, University Park, Nottingham NG7 2RD, UK*
[27]*Department of Physics and Astronomy 'Augusto Righi' (DIFA), University of Bologna, Via Gobetti 93/2, I-40129 Bologna, Italy*
[28]*INAF–Osservatorio di Astrofisica e Scienza dello Spazio, Via Gobetti 93/3, I-40129 Bologna, Italy*
[29]*CAS Key Laboratory for Research in Galaxies and Cosmology, Department of Astronomy, University of Science and Technology of China, Hefei 230026, People's Republic of China*
[30]*School of Astronomy and Space Sciences, University of Science and Technology of China, Hefei, Anhui 230026, People's Republic of China*
[31]*Institute of Deep Space Sciences, Deep Space Exploration Laboratory, Hefei 230026, People's Republic of China*
[32]*Institute of Astronomy, University of Cambridge, Madingley Road, Cambridge CB30HA, UK*
[33]*Departamento de Fisica, Universidad de Oviedo, C. Federico Garcia Lorca 18, E-33007 Oviedo, Spain*
[34]*Instituto Universitario de Ciencias y Tecnologas Espaciales de Asturias (ICTEA), C. Independencia 13, E-33004 Oviedo, Spain*
[35]*Department of Astronomy, University of Maryland, College Park, MD 20742, USA*

[36]*Instituto Nacional de Astrofísica, Óptica y Electrónica, Tonantzintla, 72000 Puebla, México*
[37]*Institute of Astronomy, Graduate School of Science, The University of Tokyo, 2-21-1 Osawa, Mitaka, Tokyo 181-0015, Japan*
[38]*Research Center for the Early Universe, Graduate School of Science, The University of Tokyo, 7-3-1 Hongo, Bunkyo-ku, Tokyo 113-0033, Japan*
[39]*Department of Astronomy, University of Cape Town, Private Bag X3, Rondebosch 7701, Cape Town, South Africa*
[40]*INAF, Instituto di Radioastronomia-Italian ARC, Via Piero Gobetti 101, I-40129 Bologna, Italy*
[41]*SISSA, Via Bonomea 265, I-34136 Trieste, Italy*
[42]*Joint ALMA Observatory, Alonso de Córdova 3107, Vitacura 763-0355, Santiago de Chile, Chile*
[43]*Sub-department of Astrophysics, University of Oxford, Denys Wilkinson Building, Keble Road, Oxford OX1 3RH, UK*
[44]*National Radio Astronomy Observatory, 520 Edgemont Road, Charlottesville, VA 22903, USA*
[45]*Max-Planck-Institut für Radioastronomie, Auf dem Hügel 69, D-53121 Bonn, Germany*

This paper has been typeset from a TEX/LATEX file prepared by the author.